PFC/JA-81-10

PROBE MEASUREMENTS OF THE BOUNDARY PLASMA IN ALCATOR C

A. J. Hayzen, D. O. Overskei and J. Moreno

Plasma Fusion Center
Massachusetts Institute of Technology
Cambridge, MA 02139

April, 1981

PROBE MEASUREMENTS OF THE BOUNDARY PLASMA IN ALCATOR C

A. J. Hayzen

South African Atomic Energy Board
Private Bag X256, Pretoria 0001
South Africa

D. O. Overskei
J. Moreno

Plasma Fusion Center
Massachusetts Institute of Technology
Cambridge, Massachusetts 02139
U.S.A.

PROBE MEASUREMENTS OF THE BOUNDARY PLASMA IN ALCATOR C

Abstract

Electron temperature, ion density and thermal flux profiles of the boundary plasma at various poloidal and toroidal locations were measured using Langmuir and thermocouple probes. The poloidal and toroidal variations of these results are then related to the various magnetic surface/limiter configurations used. The density scrape-off thickness was found to be 3mm at a toroidal field of 60 KG and the perpendicular diffusion coefficient to be of the order of Bohm diffusion.

Introduction

The main plasma column of a tokamak is usually bounded by limiters and hence the shape of the plasma is determined, not only by the magnetic surface configuration, but also by the limiters. This combination of magnetic surface and limiter configuration led to a non-uniform poloidal thermal flux loading on the Alcator C limiters.

We report here measurements of the boundary plasma (limiter shadow region) properties obtained from Langmuir and thermocouple probes at a number of different poloidal and toroidal locations and estimate perpendicular diffusion coefficients and density e-folding or scrape-off thicknesses. The results were recorded for the same plasma conditions, but the number of limiters and direction of the toroidal magnetic field relative to the plasma current were varied. This resulted in different magnetic surface/limiter configurations which affected the plasma parameters in the boundary region.

The observed results can be explained in terms of these different magnetic surface/limiter configurations. The density scrape-off thickness was found to be approximately 3mm at a toroidal field of 60KG and the perpendicular diffusion coefficient to be of the order of Bohm diffusion. The ratio of the thermal flux parallel and anti-parallel to the plasma current varied between 0.25 and 8, again consistent with the magnetic surface/limiter configurations.

Experimental Description

Two types of diagnostics were used to measure the properties of the boundary plasma in Alcator C (Fig. 1): a) A thermocouple array (electrically floating) on the bottom of F port (Fig. 2) consisting of 12 blocks of stainless steel (17x5x5mm) with a K type thermocouple inserted in the center of each block. Double blocks at two poloidal locations (-5.7° and 28.5°) allowed one to obtain toroidal heat flux information. The average thermal flux can be determined on each block by dividing the energy deposited by the discharge length and total surface area normal to the field lines; b) Combination Langmuir/thermocouple probe assemblies (Fig. 2) on the bottom of A and D ports and two on the top of F port as shown in Figure 1. The Langmuir probe tips consisted of a spherical 1 mm diameter molybdenum ball which was continuously swept from typically -60V to +10V every 10 msec during the discharge.

All thermocouples were connected to a data logger which recorded temperatures before and after a plasma shot with a one second time resolution.

The limiters on ports B and E (Fig. 1) are identical complete circular limiters consisting of 21 shaped molybdenum blocks which are electrically floating. The limiter inner surface has a radius of 16 cm; with a radial extent of $\sim$ 2.5 cm. The radius of the vacuum vessel is 19 cm. Virtual limiters consisting of annular rings of stainless steel having an inner radius of 18 cm, outer radius of 19 cm, thickness of 3 mm, are welded to the vacuuum vessel at ±4° and ±8° toroidally

from the diagnostic port center lines.

Data Analysis

Since the electron and ion gyroradii and Debye lengths are small compared to the probe dimensions, simple probe theory was used to analyse the data. The ion density was inferred from $n_i = 2I_{io}/q\bar{V}_i A$ where I_{io} is the ion saturation current, q is the ion charge, $\bar{V}_i$ is the average ion velocity and A is the cross-sectional probe area perpendicular to the magnetic field. The ions are assumed to strike the probe with the electron energy[1] so that $\bar{V}_i = (2KT_e/M)^{\frac{1}{2}}$, where KT_e is the electron energy and M the ion mass. The electron temperature is calculated by fitting $I_p = I_{io} + I_{eo} \exp(eV/KT_e)$ to the measured current-voltage characteristic, where V is the probe voltage, I_p the probe current and I_{eo} a constant. The thermal flux for a floating probe was calculated using

$$\Gamma = \frac{1}{\tau A} \int_o^\tau 2I_{io}(t)T_e(t)dt \qquad (1)$$

where τ is the plasma pulse length and we have assumed that the electrons and ions strike the probe with the same energy[1].

The thermal flux to the thermocouple blocks was calculated assuming that the energy was distributed equally on either side of the blocks perpendicular to the magnetic field. In practice, this is not true as we shall show later, but as we do not know what the ratio of the thermal flux is on either side of the blocks at all poloidal locations, we are forced

to take an average. Experimentally it was observed that the blocks reached their maximum temperature approximately 1 sec after the discharge. This enabled one to get an estimate of the radiation losses which at most accounted for 5% of the total energy absorbed by the block. Conduction losses were assumed to be negligible due to the good thermal insulation of the blocks from their support.

Results

All the results presented in this paper were taken with hydrogen discharges (Fig. 3) with the following typical parameters: plasma current I_p = 300 KA, line average density $\bar{n}_e = 2 \times 10^{14} cm^{-3}$, toroidal magnetic field B_T = 60 KG, central electron temperature T_{eo} = 1 KeV, pulse length of 300 msec and q at the limiter approximately 4. It is important to note that the horizontal position was feedback controlled to within $\simeq$ 1 mm of the center of the vacuum vessel with possible radial excursions of 3 mm during the current rise and termination phase. At the time of these measurements the vertical position was pre-programmed and could have varied by as much as 5 mm during the discharge.

Figure 3 shows the time evolution of a typical discharge. During the current rise phase the line average density rises linearly reaching an approximate constant value at about 150 msec. During the time period of 150-200 msec the plasma current and line average density remain relatively constant and the central soft X-ray detector displays typical saw-tooth activi-

ty. The saturated ion current drawn by a langmuir probe follows the line average density in time illustrating that the density in the limiter shadow region is approximately linearly related to the bulk plasma density. However, the electron temperature in the boundary region remained constant throughout the discharge.

Figure 4 shows various theoretical curves for the radial density profile of the discharge column with a line average density of $2 \times 10^{14} cm^{-3}$. The best fit[2] to the data for internal density measurements ($0 \leq r \leq 16$ cm) is typically given by curve "a". The measured density (dots) in the boundary region agrees reasonably well with the fitted profiles.

The electron temperature and ion densities presented below were averaged over the time interval of 150-200 msec, when the plasma current and density were approximately constant (Fig. 3). The ion density was measured as a function of the minor radius between the inner edge of the limiter (16 cm) and the vacuum vessel wall (19 cm). Three different cases are presented:

Case 1: limiters on B and E ports with the toroidal magnetic field, B_T, parallel to the plasma current, I_p, i.e., $B_T \parallel I_p$.

Case 2: B port limiter only with $B_T \parallel I_p$.

Case 3: B port limiter only and the direction of the toroidal magnetic field reversed relative to the plasma current, i.e., $B_T \nparallel I_p$.

These three sets of data are shown in Figures 5 and 6 for the probes on the bottom of A and D ports respectively. Similar results for the probes on the top of F port are not shown as they do not present any new information. The approximate density e-folding distance for both A and D ports is 3 mm with an exception of 13 mm at A port for Case 3. This discrepancy will be discussed later in the appendix. At D port the density for Case 2 was too high to be measured (probe current too high) between the limiter and virtual limiters. This will be discussed in the appendix.

Between the virtual limiters and vacuum vessel wall (18-19cm) the results are more difficult to interpret due to the close proximity of the virtual limiters and are therefore ignored.

The shadow election temperatures measured at D port (Fig. 7) are representative of all four probe locations, i.e., A and D bottom and the two probes at the top of F port. The electron temperature varied between 10 and 20 eV in this region without any observable systematic trend.

The thermal flux at ports A and D bottom and the two probe positions on F top was measured using the thermocouple probes described earlier. These thermocouple probes were positioned on either side of the langmuir probe (Fig. 2) such that data from all three could be used to calculate the thermal flux on approximately the same magnetic flux surface. The results obtained at A port (Fig. 8) are representative of all four thermocouple/langmuir probe assemblies. The thermal flux is plotted as a function of the minor radius between the inner edge of the

limiter and vacuum vessel wall and then compared to the average thermal flux calculated from the langmuir probe data using Equation 1. The good agreement between the measured and calculated heat flux is consistent with a thermal plasma in the limiter shadow region.

Discussion

Most of the preceding results can be interpreted in terms of the shape of the magnetic surfaces relative to the inner surface of the poloidal limiters on B and E ports. In order to do this, it is important to note that the poloidal direction of the magnetic lines of force (Fig. 12), and therefore the poloidal direction of the thermal flux, reverses when the direction of the toroidal magnetic field B_T is reversed relative to the direction of the plasma current I_p.

Another important point to note is that the shape of the outer magnetic surfaces change (Figs. 13 and 14) when the toroidal magnetic field is reversed. This is due to there being a single uncompensated toroidal turn arising from the toroidal field magnet coil, i.e., there is a single toroidal current loop of 80 KA (toroidal magnetic field B_T = 60 KG) either parallel or anti-parallel to the plasma current (I_p = 300 KA). The magnetic surfaces shown in Figures 13 and 14 were calculated using a numerical code which takes into account this single current loop as well as the appropriate vertical and horizontal equilibrium fields for the typical discharges

used for this study. These numerically calculated magnetic surfaces correspond well with the experimentally determined plasma center and outer flux surface. The main difference to note between these two sets of magnetic surfaces is that when the toroidal field B_T is parallel to the plasma current I_p the outer magnetic surfaces are elliptical, and are narrower in the horizontal plane thereby leaving a gap between the inner edge of the limiter and the outermost magnetic surface both on the inside and outside of the torus (Fig. 13). For the case of the reversed toroidal magnetic field, i.e., $B_T \nparallel I_p$, the outer magnetic surfaces are almost circular in shape and more closely follow the inner surface of the limiter.

By mapping magnetic lines of force, which just miss the limiters, onto the port at which probe measurements are taken, one can see that the magnetic field lines can carry the plasma well into the limiter shadow at that particular port. Furthermore, the distance that the plasma is carried out into the limiter shadow region varies as one either changes the number of limiters, or as one changes the direction of the toroidal magnetic field, which comprise the three cases studied. Moreover, the distance the plasma is carried into the limiter shadow or back inside the plasma bulk also depends on the plasma flow, i.e., parallel or anti-parallel to the plasma current direction. A detailed analysis of these magnetic surface/limiter configurations is given in the Appendix.

The density profiles at D port (Fig. 6) are consistent with the above type of analysis, i.e., the density profiles

for Cases 1 and 3 should qualitatively be the same since the magnetic field lines carry the plasma into the limiter shadow approximately the same distance in each case. However, for Case 2 the magnetic field lines which just miss the limiter at B port will have extended considerably into the limiter shadow at D port resulting in a dramatically higher density for a given radial position, as is clearly shown in Figure 6. Assuming that the density gradient in the region between the limiter edge and virtual limiters (16-18 cm) for Case 2 is the same as for Cases 1 and 3, one can estimate the difference in the distances which the magnetic lines of force have carried the plasma into the limiter shadow to be approximately 10 mm as shown in Figure 6. This is entirely consistent with the numerically calculated magnetic surfaces, Figures 13 and 14.

Using similar arguments as above one can also explain the density profiles taken at A port (Fig. 5). The density e-folding distance of 13 mm for Case 3 will be explained in the Appendix.

Further analysis of the results indicates that the density profiles at A port (Fig. 5) for Cases 1 and 2 should be approximately the same as the density profiles at D port for Cases 1 and 3, since the distances that the magnetic lines of force carry the plasma into the limiter shadow are approximately the same in each case. This is true if one compares the appropriate density profiles shown in Figures 5 and 6.

We will now turn our attention to the estimation of the perpendicular diffusion coeeficient. In the plasma boundary region the density gradient can be written as

$$\nabla_\perp n_i = (-1/\lambda_\perp) n_o \exp\left(\frac{r_o - r}{\lambda_\perp}\right)$$

where $\lambda_\perp$ is the density e-folding or scrape-off thickness and r_o is the limiter radius or position of the relevant magnetic surface in the limiter shadow region.

Neglecting source terms the diffusion equation can be written as

$$\nabla(\Gamma_{||} + \Gamma_\perp) = 0$$

where

$$\Gamma_{||} = nV_s/2$$

and

$$\Gamma_\perp = -D_\perp \nabla_\perp n \qquad (2)$$

where V_s is the ion sound speed. The above equations give a perpendicular diffusion coefficient[3],

$$D_\perp = \frac{V_s \lambda_\perp^2}{2\lambda_{||}} \quad ,$$

where $\lambda_{||}$ is the distance travelled parallel to the magnetic field from the limiter. Depending on the magnetic surface/limiter configuration $\lambda_{||}$ will in general differ for flow parallel or anti-parallel to the plasma current.

The scrape-off thickness in the boundary plasma was found to be approximately 3 mm (Figs. 5 and 6) excluding the exception of 13 mm at A port which we shall discuss in the Appendix. Selecting the appropriate magnetic surface/limiter configurations (Figs. 16, 17 and 18) gives an average distance of

$64 \times \pi/2 = 100$ cm for $\lambda_{||}$. This is approximately 10 mean free paths for electron-ion collisions, and gives a perpendicular diffusion coefficient, assuming $T_e = 20$eV of

$$D_{\perp} = 2.25 \times 10^3 cm^2 S^{-1}$$

For comparision

$$D_{Bohm} = 2 \times 10^3 cm^2 S^{-1}$$

$$D_{Classical} = 6 cm^2 S^{-1}$$

The observation that the deduced perpendicular diffusion coefficient in the limiter shadow is approximately equal to Bohm is consistent with results obtained on other tokamak devices[1,3-7].

We will now discuss the results obtained with the thermocouple array on the bottom of F port.

This array (Fig. 2) allowed measurement of the poloidal variation of the thermal flux from $-17.5° \leq \theta \leq +40.5°$ at various minor radii in the limiter shadow region. This particular range in θ was chosen for two reasons: a) limiting access through the bottom of F port and, b) to coincide poloidally with the thermal damage that had previously been observed on the F port virtual limiters, which suggested some non-uniform poloidal variation of thermal flux. Figure 9 shows the poloidal variation of the measured thermal flux at r = 17.7cm, just beyond the virtual limiters at r = 18cm, for the three cases considered. A peak at a poloidal angle of approximately 8° close-

ly corresponds to the location of maximum erosion of the virtual limiters. All three cases exhibited roughly the same poloidal variation, but the absolute value of the thermal flux increased dramatically for Case 2.

Toroidal drift variation of the thermal flux (i.e., parallel and anti-parallel to the plasma current) was measured at two poloidal locations (θ = -5.7° and +28.5°) with separate thermocouple blocks facing in opposite toroidal directions (Fig. 2). The results are shown in Figures 10 and 11 where we have plotted the ratio of the thermal flux in the anti-parallel direction to that in the parallel direction as a function of radial position. Large asymmetries in the toroidal thermal flux are clearly evident. For a given radial location the ratio of energy deposited on the anti-parallel to the parallel side varied from 0.5 (Case 3) to 4.2 (Case 1). Moreover, this ratio varied by as much as a factor of 3 as one traversed the boundary plasma radially, with $\Gamma_{\#}/\Gamma_{||}$ approaching 3 at the limiter plasma boundary (r = 16cm). These observations are reasonable considering the shape of the outer magnetic flux surfaces as we will now discuss. If one maps the magnetic surface/limiter configurations applicable to F port, then one sees that the thermal flux can, under certain circumstances, be carried out further in one toroidal direction (say parallel to I_p) than in the other toroidal direction (anti-parallel to I_p). Therefore, at a fixed radial position, the thermal fluxes will not be equal, thereby giving a ratio which is not equal to one. (See the Appendix for details.) The results shown in Figures 10 and 11 are consistent with this analysis.

Appendix

It was pointed out earlier in the discussion of the results that the poloidal rotation of the magnetic field lines reversed (Fig 12) when the direction of the toroidal magnetic field was reversed relative to the direction of the plasma current. It was also pointed out that the shape of the magnetic surfaces change (Figs 13 and 14) when the toroidal magnetic field is reversed. Keeping these two variations in mind, it can be shown that the density profiles at D port (Fig 6) can be explained by mapping the magnetic surfaces, which just miss the limiters, onto D port (Figs 15, 16, and 17).

To see this more clearly, consider figure 15. The dashed line represents the outermost magnetic surface that just misses the limiter on B port everywhere. This surface qualitatively has the same shape as those calculated numerically in figure 13. The semi-circular solid line marked "limiter shadow" is the shadow of the inner edge of the limiter at B port projected onto D port. D port is 120° away from B port toroidally in the plasma current direction (Fig 1), and -240° toroidally in the anti-parallel direction. If we now assume that q = 4 at the limiter, then, mapping a magnetic line of force from the limiter at B port onto the Langmuir probe at D port in the anti-parallel direction gives a poloidal rotation of -240/4 = -60°. When the toroidal magnetic field is parallel to the plasma current ($B_T \parallel I_p$) the poloidal rotation of the magnetic line of force (Fig 12) is in the anti-clockwise direction when look ng in

the plasma current direction. If we now assume that this magnetic line of force leaving the limiter at point A (Fig. 15) is approximately parallel to the outer magnetic surface (dashed line) then we see that by the time this magnetic line of force reaches D port it has moved into the limiter shadow to point A'. Similarly if we consider a magnetic line of force in the parallel direction then it rotates 120° in the toroidal direction (Fig. 1) and therefore, if q = 4, 120/4 = 30° in the poloidal direction, and in this case the poloidal rotation (Fig. 12) is clockwise. Furthermore, due to the particular shape of the magnetic surface (Fig. 15) it moves from point B to B' and thus further into the bulk of the plasma and not into the limiter shadow region. Neglecting effects due to diffusion, the thermal plasma flux moving in the anti-parallel direction, that just misses the limiter at B port moves well into the limiter shadow by the time it gets to D port.

However, when there are limiters on both B and E ports, a magnetic line of force that just misses the limiter at B port in the anti-parallel direction moves into the limiter shadow region and is intercepted by the limiter at E port. Therefore, the distance that the magnetic lines of force carry the plasma into the limiter shadow at D port is controlled by the limiter at E port for the anti-parallel direction. A field line missing the E port limiter experiences a poloidal rotation of 60/4 = 15° going from ports E to D, i.e., from point A to A' in Figure 16. The poloidal rotation for the

parallel case is unchanged (30°) as the limiter at E port does not affect it. The net result is that less plasma is carried a shorter distance into the limiter shadow as compared to the case of a single limiter at B port (Fig. 15).

When the direction of the magnetic field is reversed ($B_T \nparallel I_p$) and with only a limiter on B port (Case 3) the shape of the magnetic surfaces change (Fig.14) with the result that the thermal flux is qualitatively carried out the same distance (Figs. 16 and 17) as with limiters on B and E ports and the toroidal magnetic field parallel to the plasma current ($B_T \parallel I_p$, Case 1).

The above results can be seen quite clearly from the density measurements taken at D port (Fig 6). The ion density radial profile in the limiter shadow region is the same for Cases 1 and 3 in agreement with the magnetic surface/ limiter configurations (Figs. 16 and 17). Furthermore, for case 2 the density is far greater at a given radius than for cases 1 and 3 again in agreement with the above magnetic surface/ limiter configurations (Fig. 15).

Similar arguments explain the results taken at A port (Figs. 16, 18, and 19). The case for which the scrape-off thickness is 13mm (Case 3) can be explained in terms of two scrape-off thickness. (Figs. 19 and 20). In the parallel direction the plasma has rotated through an angle of 300 degrees toroidally giving a scrape-off thickness of approximately 5mm

using equation 2 and assuming $D_\perp = 2 \times 10^3 cm^2 S^{-1}$. If one further assumes that the magnetic surface has carried the plasma out 1 cm (Fig. 19) and that the density is constant in this region (16-17cm) then one gets curve "a" in Figure 20. In the anti-parallel direction the plasma has only rotated through an angle of 60 degrees toroidally giving a scrape-off thickness of approximately 3mm assuming $D_\perp = 2 \times 10^3 cm^2 S^{-1}$. If we now assume that the magnetic surfaces have not carried the plasma out beyond the limiter edge (Fig. 19), we then get curve "b" on Figure 20. Adding the parallel and anti-parallel density profiles (curves "a" and "b") results in a total density represented by the dots in Figure 20, with an approximate scrape-off thickness of 9 mm, closely approximating the 13 mm scrape-off thickness observed at A port (Fig. 5) for Case 3.

If one compares Figures 16, 17, and 18, one sees that the distance the magnetic lines of force carry the plasma into the limiter shadow is approximately the same in each case. Therefore, one would expect the density profiles to be approximately the same at A and D ports for these four cases. Comparing the density profiles in figures 5 and 6 confirm this observation.

Figures 21, 22, and 23 show the magnetic surface limiter configuration at the bottom of F port for the three cases indicated. This corresponds to the position of the thermocouple array (Fig. 2). The important point to note here is that the

plasma can be carried into the limiter shadow in one direction and not in the other. This results in the ratio of the thermal flux parallel to the anti-parallel direction being unequal to one at a given radial position.

The variation of this ratio with radial position, for example case 1 in Figure 10, can also be explained in terms of the magnetic surface/limiter configurations. Consider the model shown in Figure 24. In the parallel direction we have a thermal flux as shown. In the anti-parallel direction the magnetic surfaces carry the plasma into the limiter shadow giving the curve shown. If we now take the ratio of these two curves (the dotted line) we get a profile similar to that shown in Figure 10. Comparing the various magnetic surface/limiter configurations applicable to the ratios shown in Figures 10 and 11 (i.e. Figs. 21, 22, and 23) this type of analysis (Fig. 24) is consistent with the results obtained.

Conclusion

There are three general conclusions one can draw from the results presented in this paper.

a) The perpendicular diffusion coefficient is of the order of Bohm diffusion,

b) For the regime considered in these experiments the plasma in the boundary region was found to be thermal i.e., no significant high energy tail and

c) The poloidal and toroidal variations of the thermal flux is non-uniform and depends on the interaction between the outer magnetic surfaces and limiters.

The main implications of these results is that the poloidal limiters should have the same shape as the outer magnetic surfaces to distribute the thermal flux evenly around the limiter. Furthermore, the more poloidal limiters there are the lower the thermal loading on each limiter. However, there will probably still be a small non-uniform thermal loading on the limiters during the plasma current rise and termination phases as the shape of the magnetic surfaces change during this time. It will also be extremely important to ensure that the plasma, and therefore magnetic surfaces, are properly centralized relative to the poloidal limiters at all times. A further implication of these results is that poloidal limiters should be more effective in distributing the thermal load than toroidal limiters, particularly if the plasma cross-section is not exactly circular. (Circular to better than one scrape-off thickness for a circular vacuum vessel). This is because the magnetic lines of force

travel around the torus 4 times, if q = 4, before intersecting a toroidal limiter and therefore allows the plasma to diffuse further, whereas they only travel around once to intersect a poloidal limiter. It is also possible that they could intersect the vacuum vessel wall rather than a toroidal limiter if the magnetic surface is badly distorted.

The above implications will be important for future generation tokamaks where the thermal wall loading could be a severe problem. It is therefore important to investigate the boundary plasma properties further, particularly in regimes other than those presented in this paper.

Acknowledgements

The authors would like to especially thank Juan Moreno and Steve Fairfax for their help in the experimental work. In addition Nick Sharky for the numerical calculations and the rest of the Alcator group for their support and information for these experiments.

REFERENCES

1) L. S. Scaturro, B. Kusse, Nuclear Fusion, Vol. 18, No. 12 (1978).

2) Paper presented at the IAEA meeting, Brussels, 1980. To be published.

3) K. Uehara et. al., Plasma Physics, Vol. 21, 1979.

4) S. Zweben, Mechanical Diverter Workshop, M.I.T., October 1980.

5) R. Budney, Mechanical Diverter Workshop, M.I.T., October 1980.

6) M. Hacker, Mechanical Diverter Workshop, M.I.T., October 1980.

7) TRF Group, Plasma Surface Interactions in Controlled Fusion Devices, Garmisch, April 1980.

Figure 1

Top view of Alcator C showing location of limiters, virtual limiters, probes and various dimensions. The direction of the toroidal magnetic field and plasma current for Case 1 are as indicated. The direction of the plasma current is unchanged for all three cases. The radial location (r) of the probe/thermocouple assemblies are indicated by the circles at ports A, D and F.

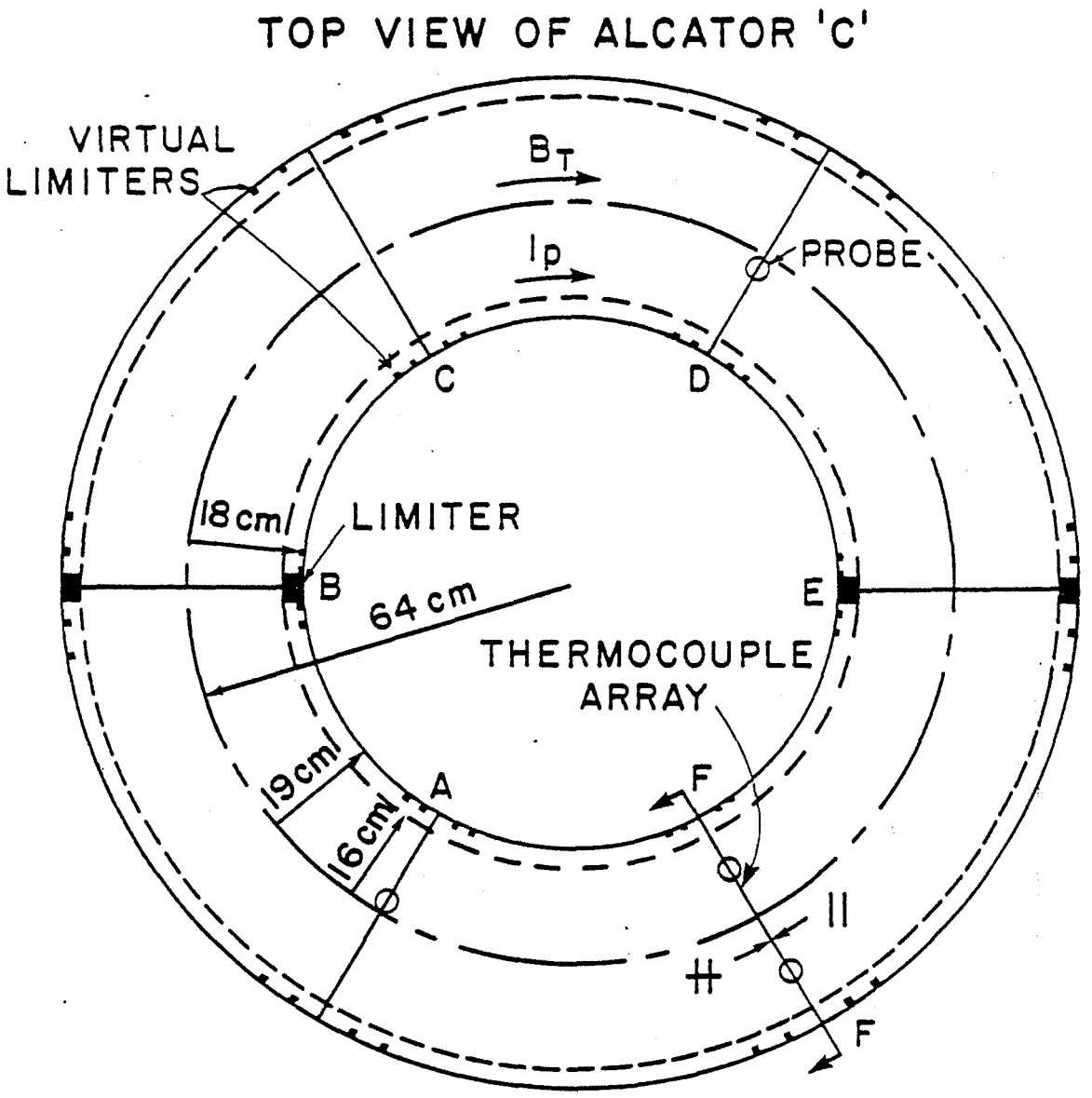
TOP VIEW OF ALCATOR 'C'
VIRTUAL LIMITERS
B_T
I_p
PROBE
C
D
18 cm
LIMITER
B
64 cm
E
THERMOCOUPLE ARRAY
19 cm
16 cm
A
F
F
F PORT CROSS-SECTION
B&E LIMITERS
B LIMITER
B LIMITER
q = 4
$B_T \parallel I_p$
$\#30° \mid \parallel 15°$
(1)
q = 4
$B_T \parallel I_p$
$\#30° \mid \parallel 60°$
(2)
q = 4
$B_T \# I_p$
$\parallel 60° \mid \#30°$
(3)
PFC-5068

FIG. 1

Figure 2

Cross-sectional view of F port (see Fig. 1) showing the array of thermocouple blocks on the bottom and the combination Langmuir probe and thermocouple blocks on the top of the port. Ports A and D bottom each have one of these Langmuir probe-thermocouple block assemblies installed as indicated in Figure 1.

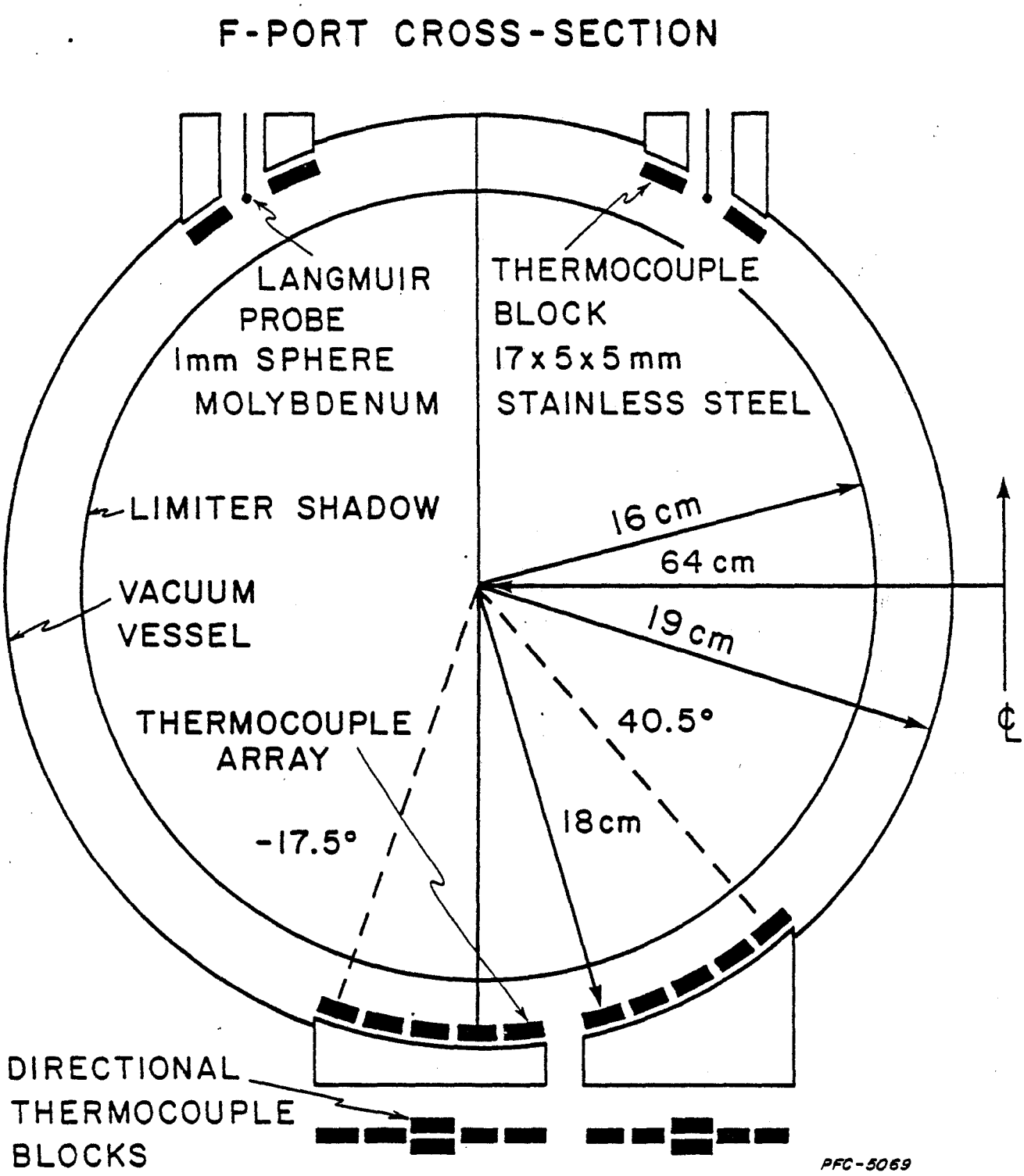
F-PORT CROSS-SECTION
LANGMUIR PROBE 1mm SPHERE MOLYBDENUM
THERMOCOUPLE BLOCK 17 x 5 x 5 mm STAINLESS STEEL
LIMITER SHADOW
VACUUM VESSEL
16 cm
64 cm
19 cm
40.5°
THERMOCOUPLE ARRAY
-17.5°
18 cm
DIRECTIONAL THERMOCOUPLE BLOCKS
PFC-5069

FIG. 2

Figure 3

Diagram showing the time evolution of plasma current, loop voltage, central soft X-ray, line average density and saturated ion current for a typical discharge using hydrogen. Peak plasma parameters are: I_p = 300 KA, $\bar{n}_e = 2 \times 10^{14} cm^{-3}$, B_T = 60 KG, T_{eo} = 1 KeV, pulse length 300 msec and q at the limiter approximately 4.

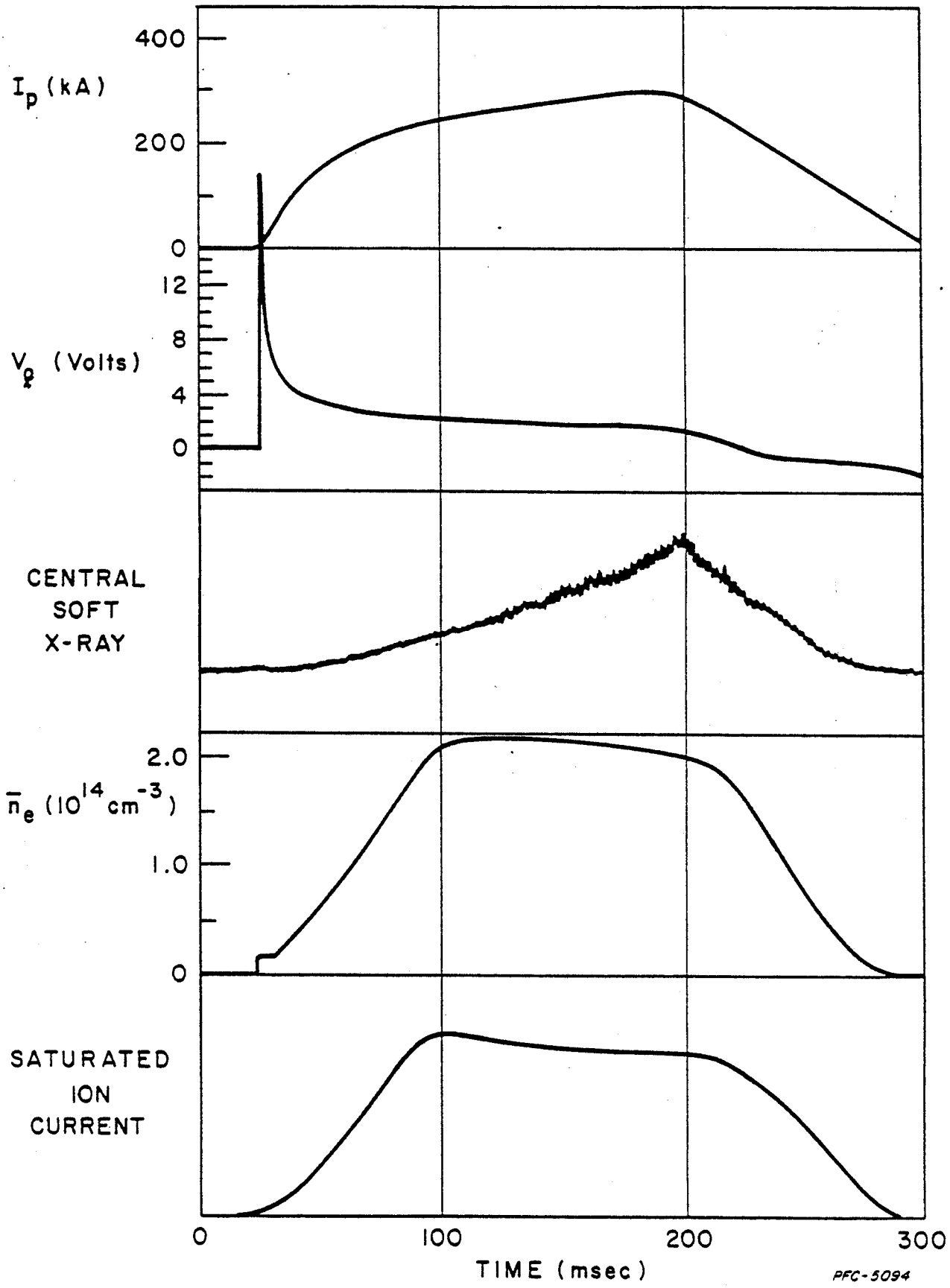
400
I_p (kA)
200
0
12
8
V_ℓ (Volts)
4
0
CENTRAL
SOFT
X-RAY
2.0
$\bar{n}_e$ (10^{14} cm^{-3})
1.0
0
SATURATED
ION
CURRENT
0
100
200
300
TIME (msec)
PFC-5094

FIG. 3

Figure 4

Typical fitted density profiles for a line average density of $2 \times 10^{14} cm^{-3}$. The dots represent the measured density profile in the boundary plasma region.

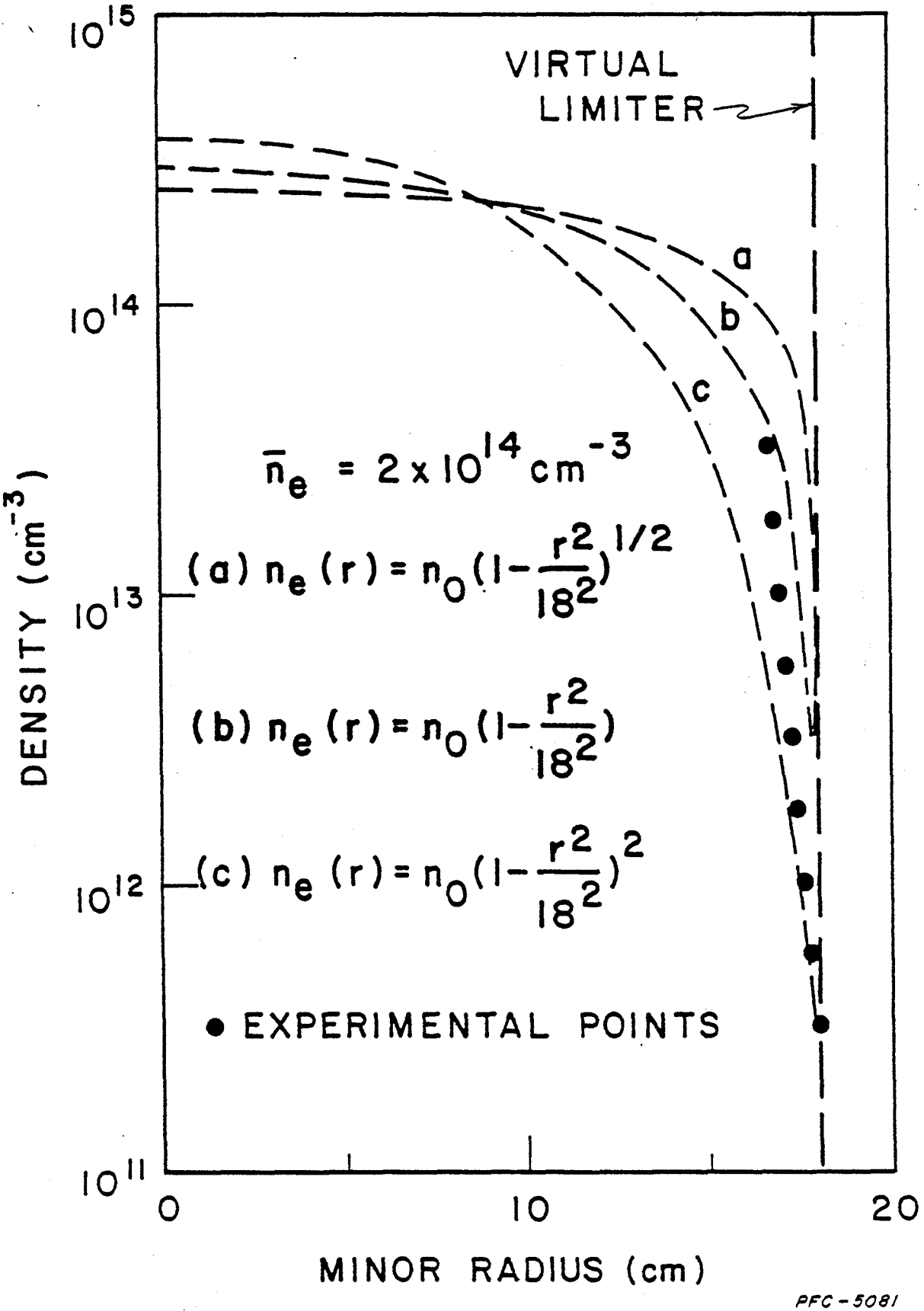
VIRTUAL
LIMITER
a
b
c
$\bar{n}_e = 2 \times 10^{14}\ cm^{-3}$
(a) $n_e(r) = n_0(1-\frac{r^2}{18^2})^{1/2}$
(b) $n_e(r) = n_0(1-\frac{r^2}{18^2})$
(c) $n_e(r) = n_0(1-\frac{r^2}{18^2})^2$
● EXPERIMENTAL POINTS
10^{15}
10^{14}
10^{13}
10^{12}
10^{11}
DENSITY (cm^{-3})
0
10
20
MINOR RADIUS (cm)
PFC-5081

FIG. 4

Figure 5

Ion density averaged over the time interval 150-200 msec as a function of minor radius between the vacuum vessel wall and the limiter edge at A port for the three cases studied. The density e-folding distance between the limiter edge and virtual limiter is approximately 3.3mm for cases 1 and 2 and 13mm for case 3.

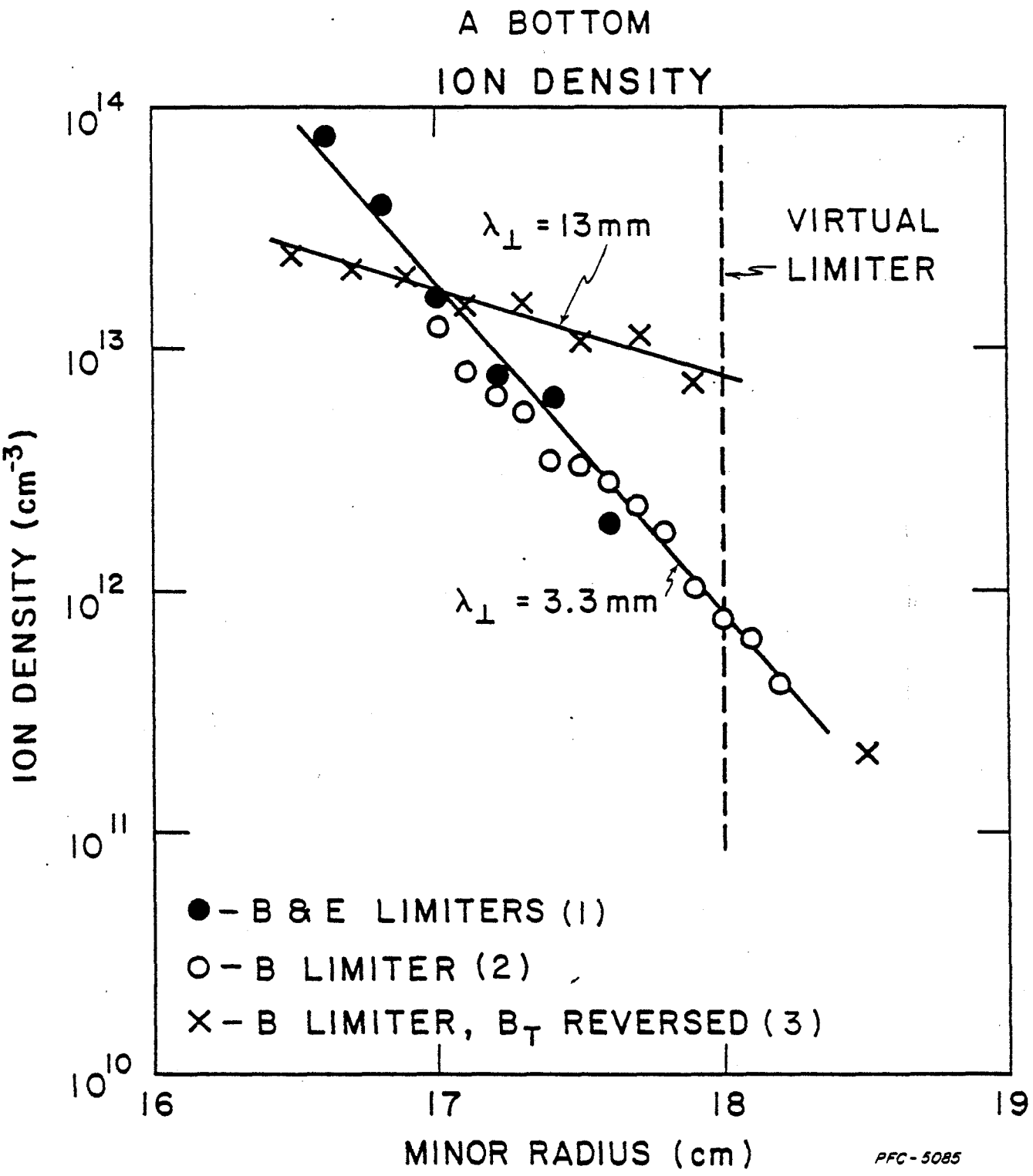
A BOTTOM
ION DENSITY
10^{14}
10^{13}
10^{12}
10^{11}
10^{10}
ION DENSITY (cm^{-3})
$\lambda_\perp$ = 13mm
VIRTUAL
LIMITER
$\lambda_\perp$ = 3.3mm
● – B & E LIMITERS (1)
○ – B LIMITER (2)
× – B LIMITER, B_T REVERSED (3)
16
17
18
19
MINOR RADIUS (cm)
PFC-5085

FIG. 5

Figure 6

Ion density averaged over the time interval 150-200 msec as a function of minor radius between the vacuum vessel wall and the limiter edge at D port for the three cases studied. The density e-folding distance between the limiter edge and the virtual limiter is approximately 2.8mm for cases 1 and 3.

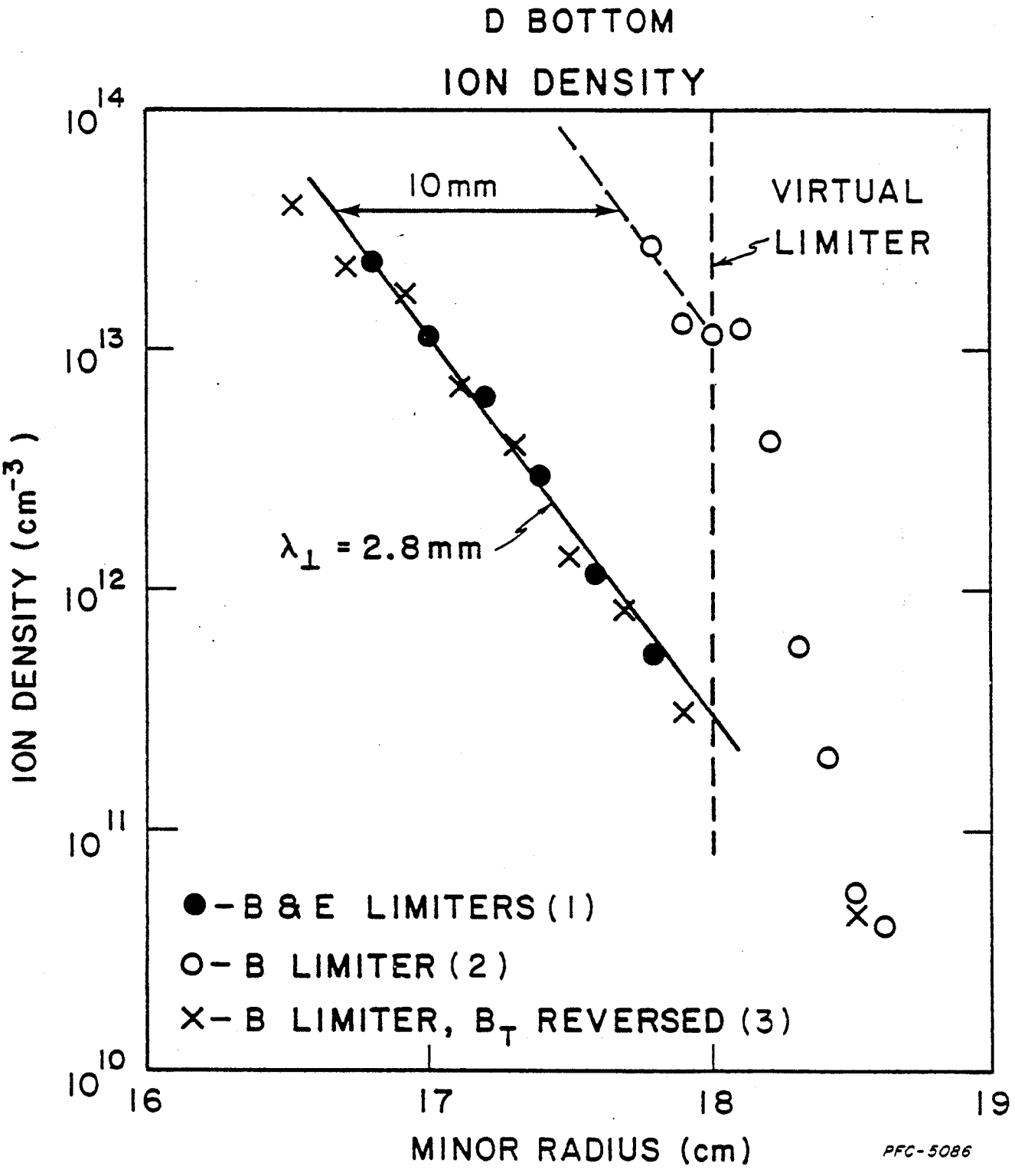
D BOTTOM
ION DENSITY
10mm
VIRTUAL
LIMITER
$\lambda_\perp$ = 2.8mm
●-B & E LIMITERS (1)
O-B LIMITER (2)
X-B LIMITER, B_T REVERSED (3)
ION DENSITY (cm^{-3})
10^{14}
10^{13}
10^{12}
10^{11}
10^{10}
16
17
18
19
MINOR RADIUS (cm)
PFC-5086

FIG. 6

Figure 7

Electron temperature averaged over the time interval 150-200 msec as a function of minor radius between the vacuum vessel wall and limiter edge at D port for the three cases shown.

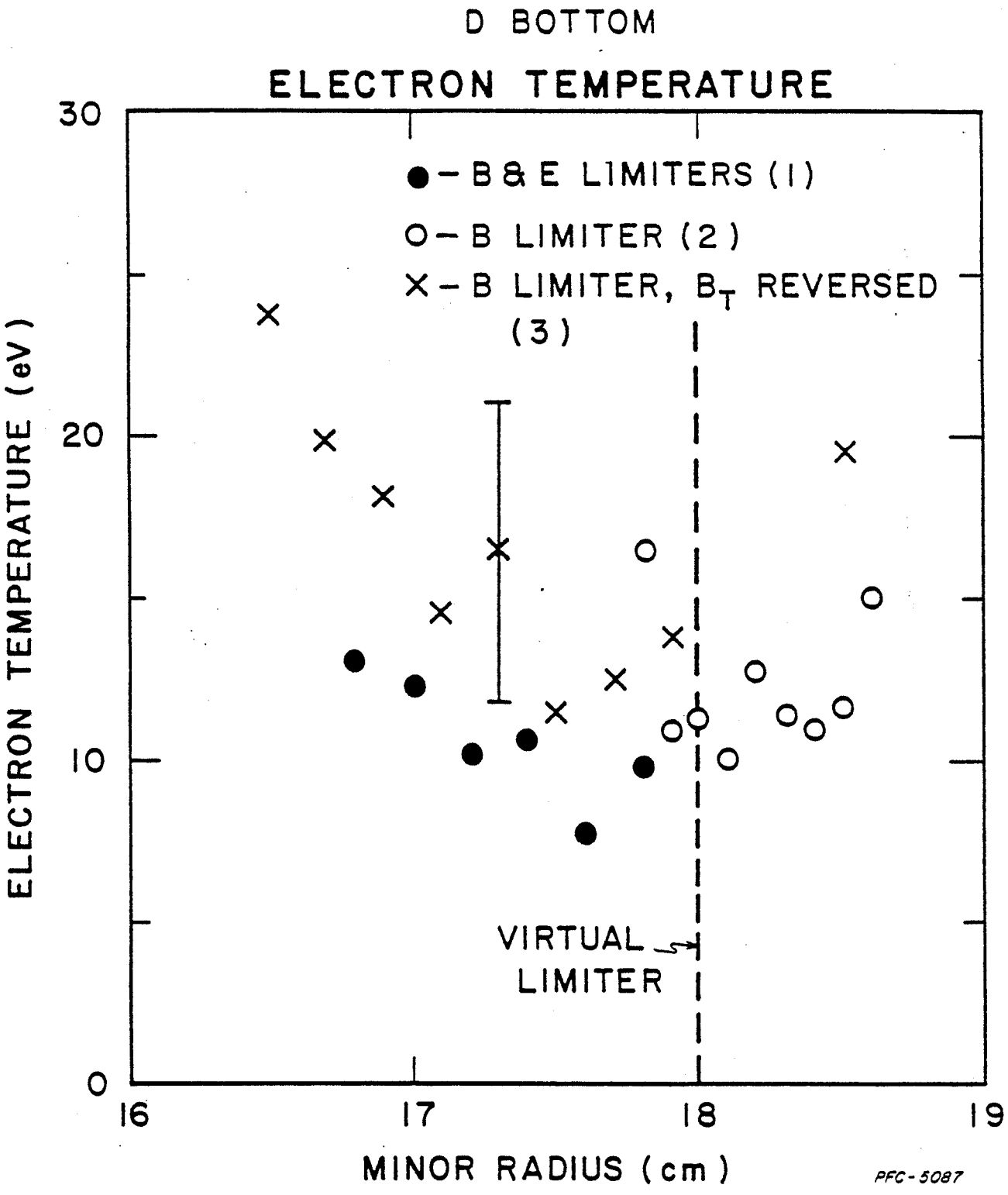
D BOTTOM
ELECTRON TEMPERATURE
30
20
10
0
● – B & E LIMITERS (1)
○ – B LIMITER (2)
× – B LIMITER, B_T REVERSED (3)
VIRTUAL LIMITER
ELECTRON TEMPERATURE (eV)
16
17
18
19
MINOR RADIUS (cm)
PFC-5087

FIG. 7

Figure 8

A comparison of the thermal flux measured by thermocouple probes and that calculated from Langmuir probe data as a function of minor radius at A port.

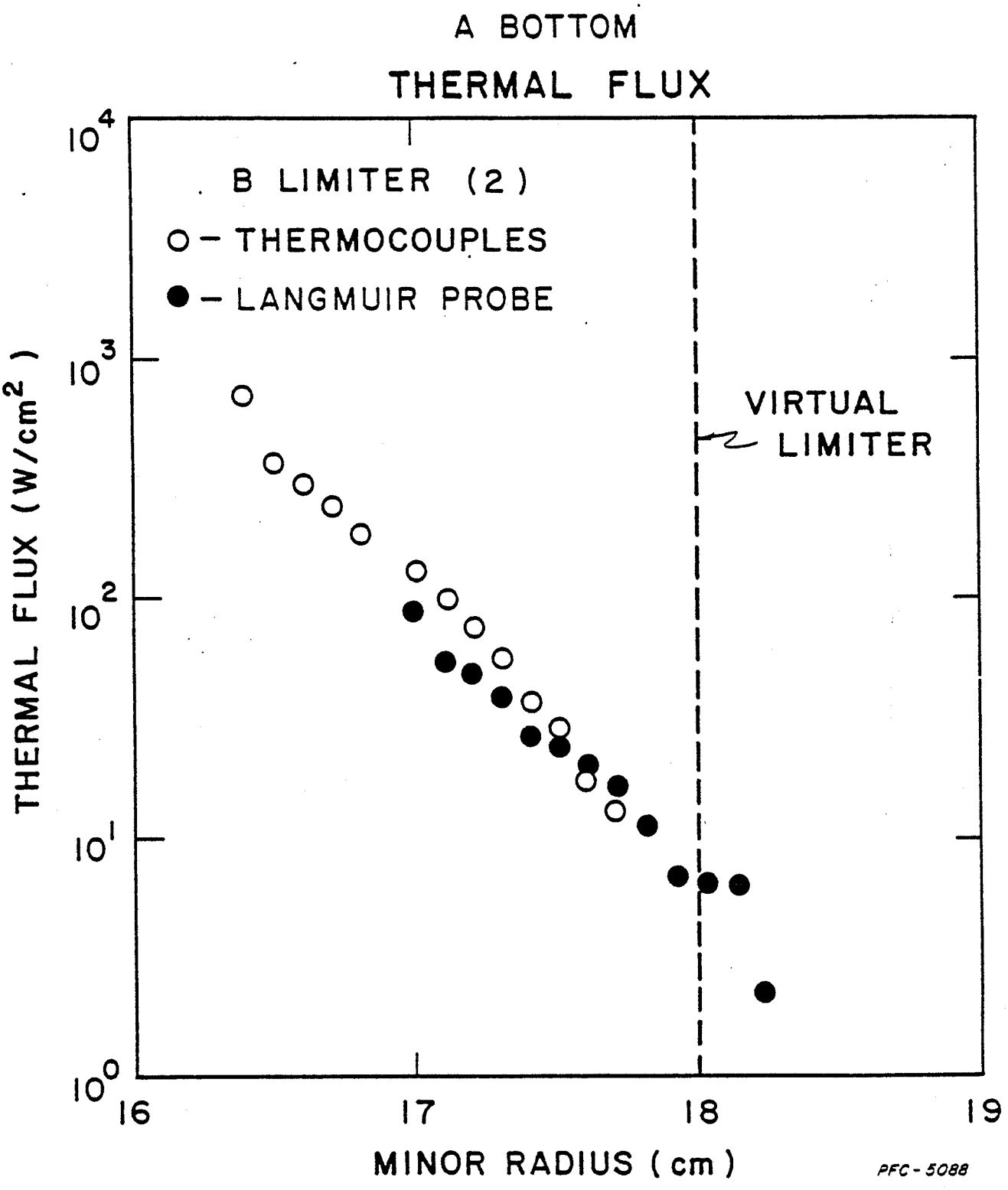
A BOTTOM
THERMAL FLUX
B LIMITER (2)
O – THERMOCOUPLES
● – LANGMUIR PROBE
VIRTUAL LIMITER
THERMAL FLUX (W/cm²)
10⁴
10³
10²
10¹
10⁰
16
17
18
19
MINOR RADIUS (cm)
PFC-5088

FIG. 8

Figure 9

Thermal flux as measured using the thermocouple array on F port as a function of poloidal angle at a minor radius of 17.7cm.

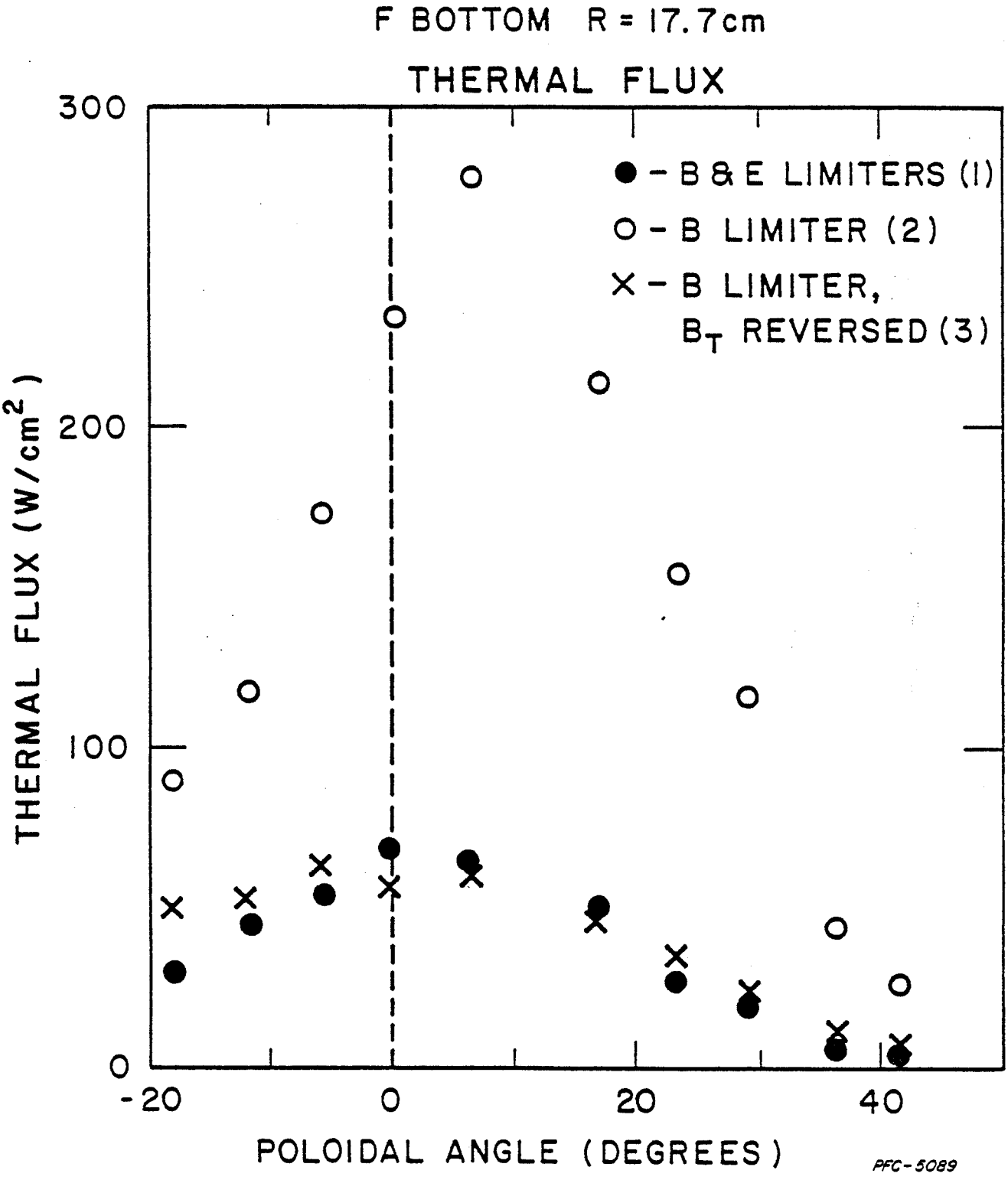
F BOTTOM R = 17.7cm
THERMAL FLUX
300
200
100
0
-20
0
20
40
● - B & E LIMITERS (1)
O - B LIMITER (2)
X - B LIMITER, B_T REVERSED (3)
THERMAL FLUX (W/cm^2)
POLOIDAL ANGLE (DEGREES)
PFC-5089

FIG. 9

Figure 10

Ratio of the thermal fluxes, measured using the thermocouple blocks, anti-parallel and parallel to the plasma current at a poloidal angle of -5.7° at F port, (see Fig. 2) as a function of minor radius in the limiter shadow region. For case 3 the ratio is inverted.

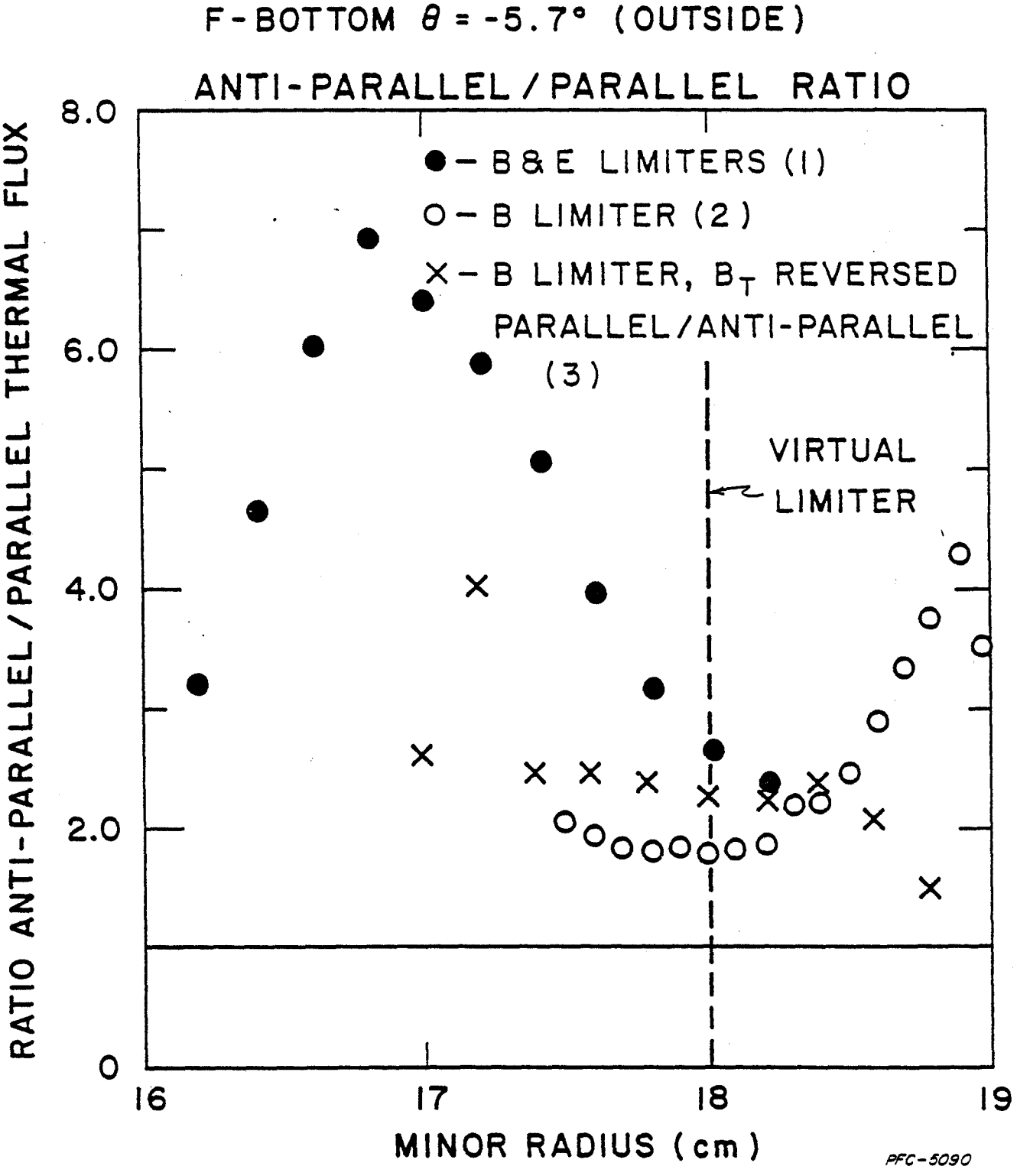
F-BOTTOM θ = -5.7° (OUTSIDE)
ANTI-PARALLEL / PARALLEL RATIO
RATIO ANTI-PARALLEL / PARALLEL THERMAL FLUX
8.0
6.0
4.0
2.0
0
16
17
18
19
MINOR RADIUS (cm)
● – B & E LIMITERS (1)
○ – B LIMITER (2)
× – B LIMITER, B_T REVERSED
PARALLEL/ANTI-PARALLEL
(3)
VIRTUAL
LIMITER
PFC-5090

FIG. 10

Figure 11

Ratio of the thermal fluxes, measured using the thermocouple blocks, anti-parallel and parallel to the plasma current at a poloidal angle of 28.5° at F port, (see Fig. 2) as a function of minor radius in the limiter shadow region. For case 3 the ratio is inverted.

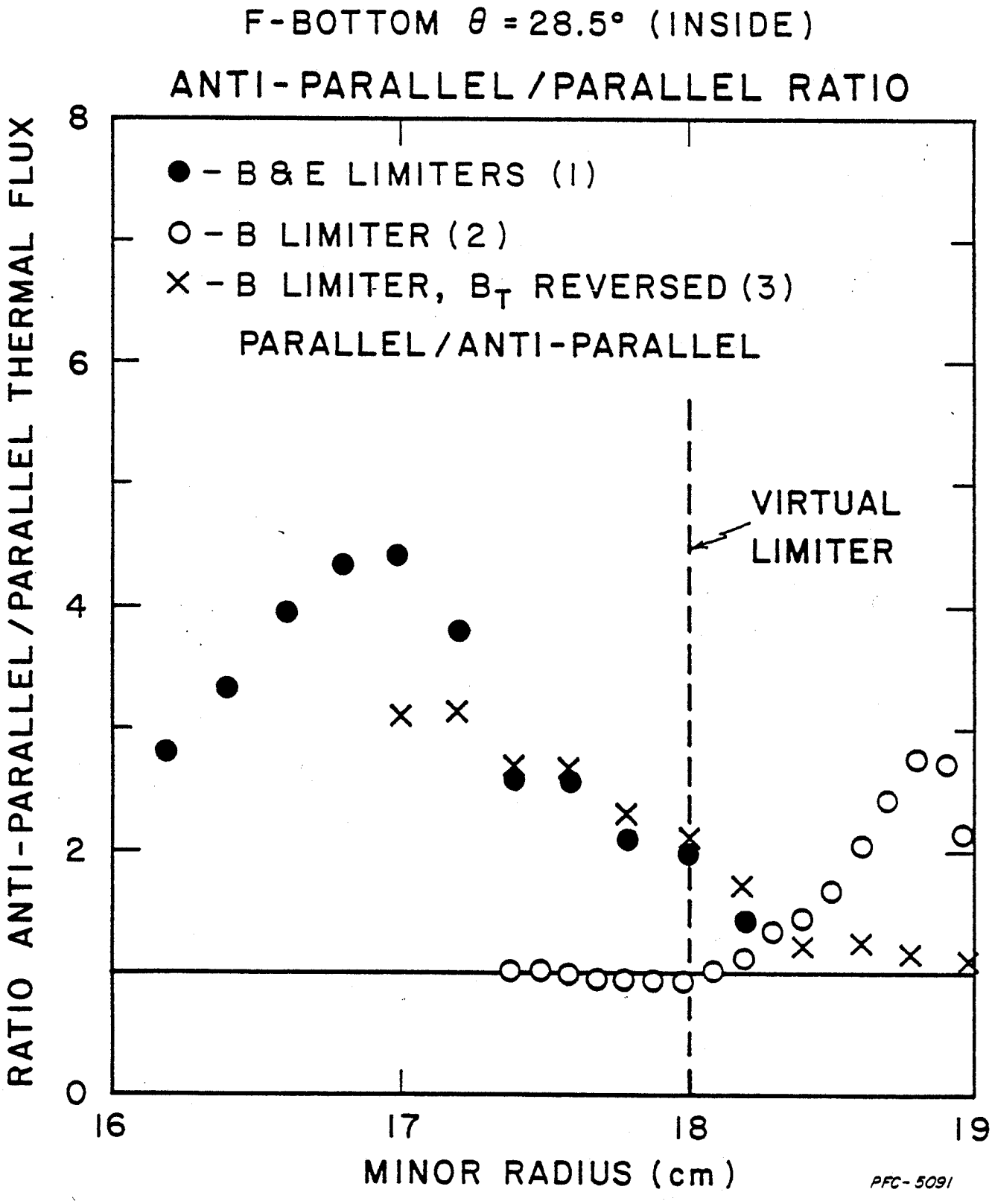
F-BOTTOM θ = 28.5° (INSIDE)
ANTI-PARALLEL / PARALLEL RATIO
● - B & E LIMITERS (1)
○ - B LIMITER (2)
× - B LIMITER, B_T REVERSED (3)
PARALLEL / ANTI-PARALLEL
VIRTUAL LIMITER
RATIO ANTI-PARALLEL / PARALLEL THERMAL FLUX
0
2
4
6
8
16
17
18
19
MINOR RADIUS (cm)
PFC-5091

FIG. 11

Figure 12

Diagram showing the poloidal rotation of the helical magnetic field lines around the torus for the two cases of toroidal magnetic field parallel and anti-parallel to the plasma current.

$B_T \parallel I_p$

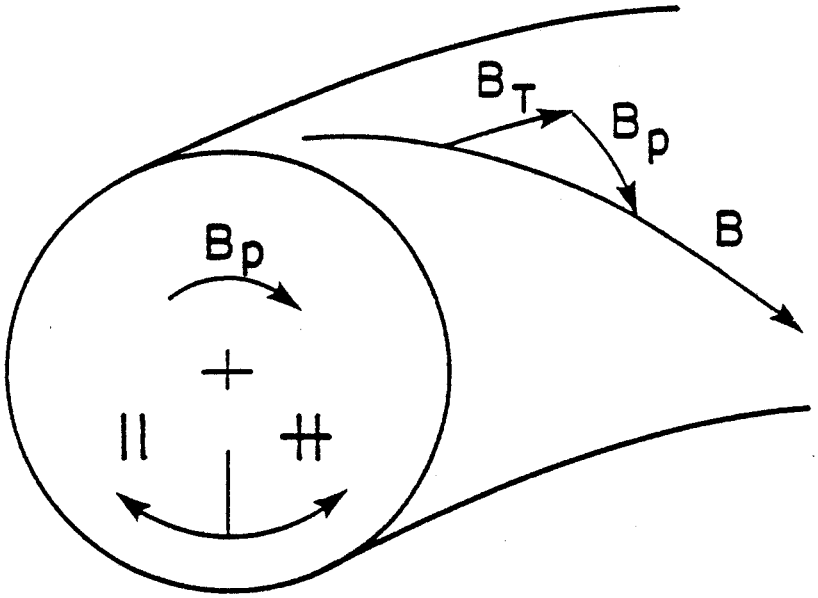

$B_T \perp I_p$

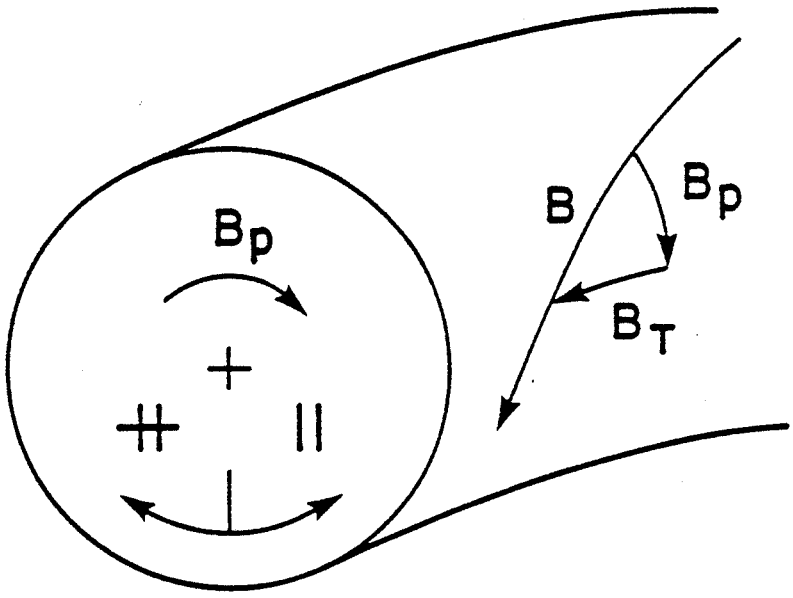

PFC-5080

FIG. 12

Figure 13

Computed equilibrium magnetic surfaces for I_p = 300KA, and B_T = 60KG for the case when the toroidal magnetic field is parallel to the plasma current. The non-circular shape of the magnetic surfaces is due to their being a single toroidal turn of the toroidal magnetic field coil which is not compensated. This results in a current loop anti-parallel to the plasma current carrying the toroidal magnetic field coil current of 80KA.

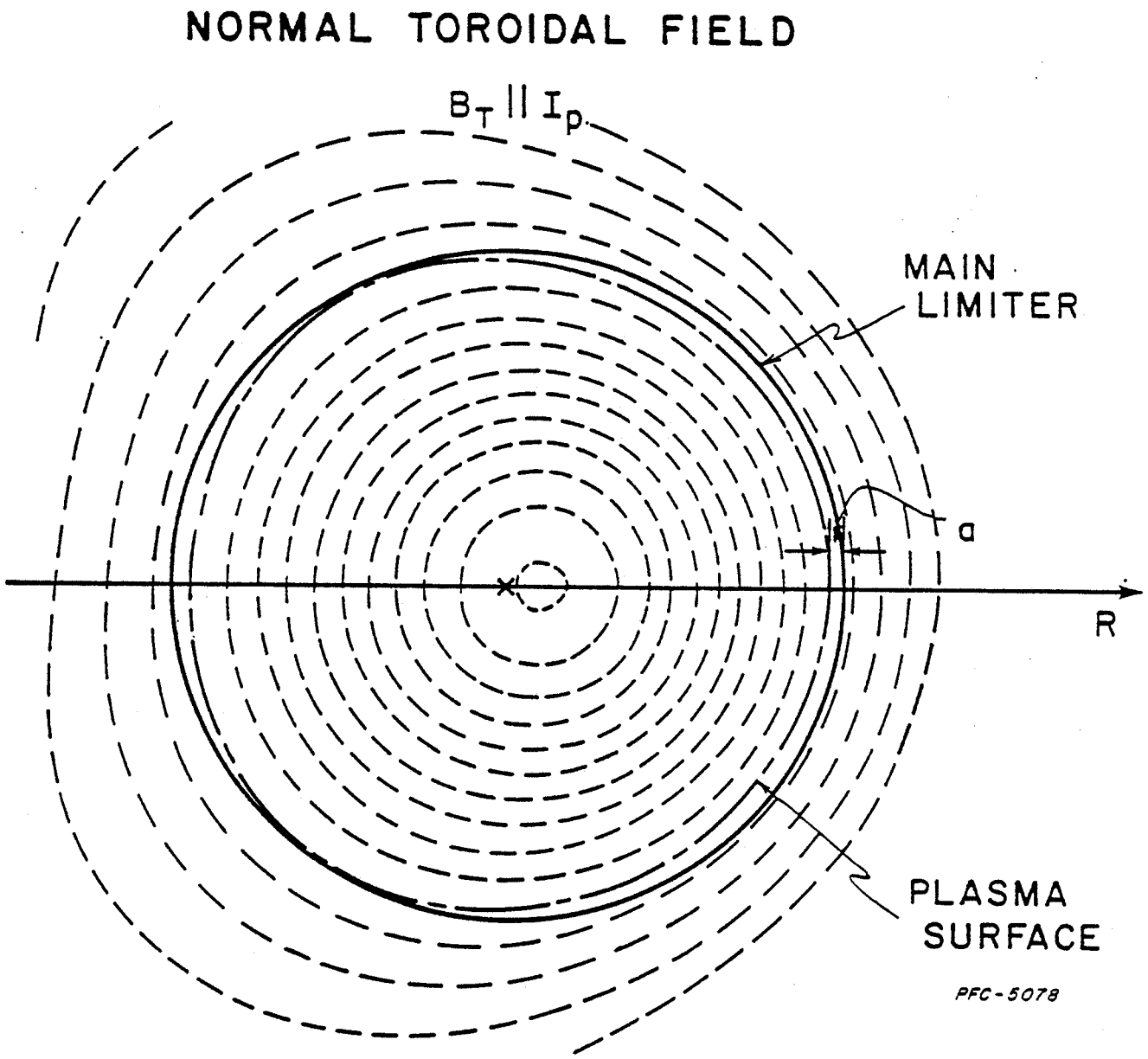
NORMAL TOROIDAL FIELD
$B_T \parallel I_p$
MAIN LIMITER
a
R
PLASMA SURFACE
PFC-5078

FIG. 13

Figure 14

Computed equilibrium magnetic surfaces for I_p = 300KA and B_T = 60KG for the case when the toroidal magnetic field is anti-parallel to the plasma current. The slightly non-circular shape of the magnetic surfaces is due to their being a single toroidal turn of the toroidal magnetic field coil which is not compensated. This results in a current loop parallel to the plasma current carrying the toroidal magnetic field coil current of 80KA.

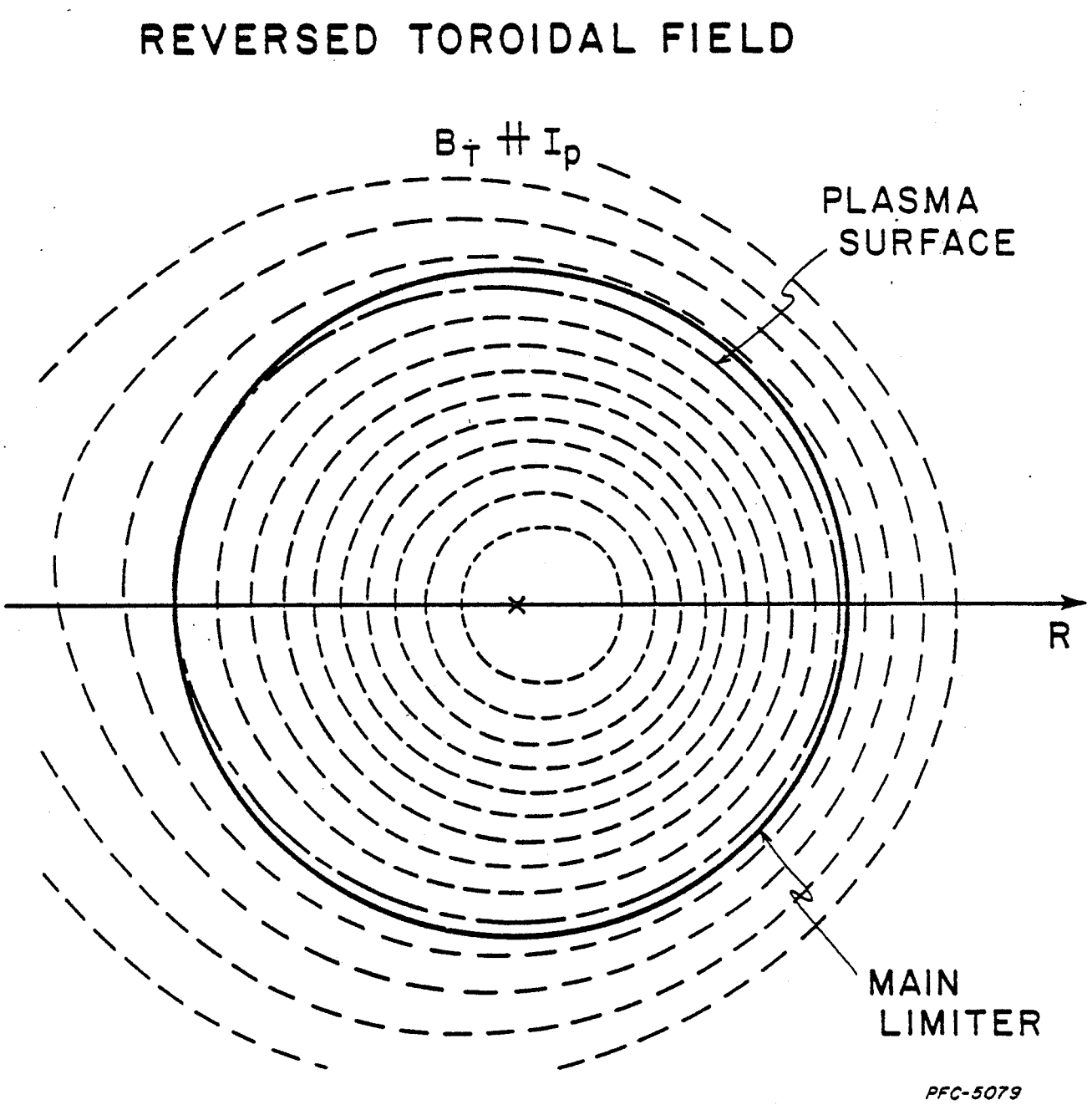
REVERSED TOROIDAL FIELD
$B_T \# I_p$
PLASMA SURFACE
R
MAIN LIMITER
PFC-5079

FIG. 14

Figure 15

Qualitative mapping of the magnetic surfaces that just miss the limiter at B port onto, D port, both parallel (30° poloidal rotation assuming q = 4) and anti-parallel (60° poloidal rotation) to the plasma current. The magnetic surfaces qualitatively have the same shape (Fig. 13) as those computed for $B_T \parallel I_p$. Neglecting diffusion it can be seen that the magnetic surfaces carry the plasma either out beyond the limiter shadow (A to A') or further into the body of the plasma (B to B') at D port depending on the poloidal location and direction of the thermal flux.

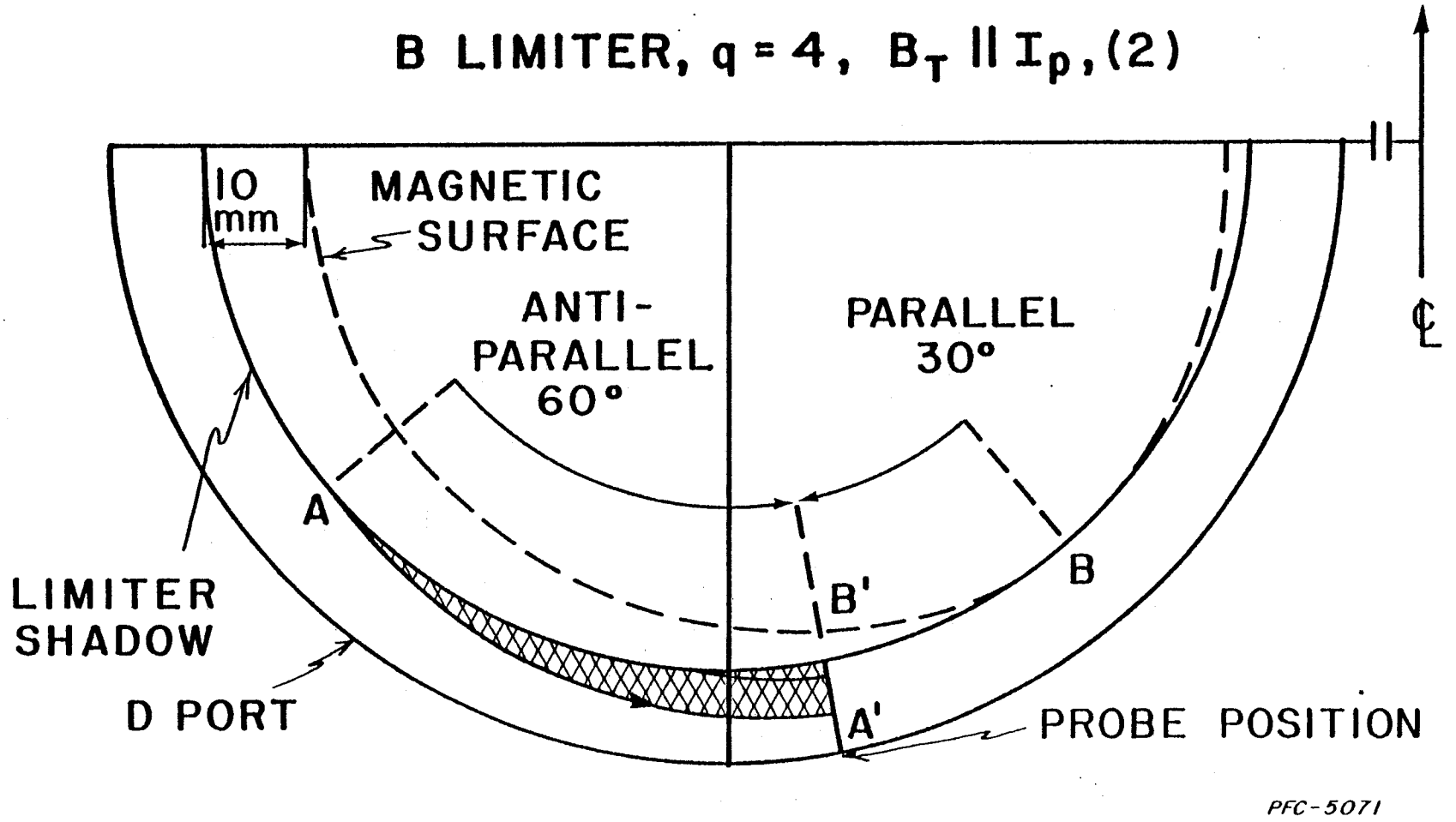
B LIMITER, q = 4, B_T ‖ I_p, (2)
10 mm
MAGNETIC SURFACE
ANTI-PARALLEL 60°
PARALLEL 30°
A
B
B'
A'
LIMITER SHADOW
D PORT
PROBE POSITION
PFC-5071

FIG. 15

Figure 16

Qualitative mapping of the magnetic surfaces that just miss the limiters at both B and E ports onto either A or D ports, both parallel (30° poloidal rotation assuming q = 4) and anti-parallel (15° poloidal rotation) to the plasma current. The magnetic surfaces qualitatively have the same shape (Fig. 13) as those computed for $B_T \parallel I_p$.

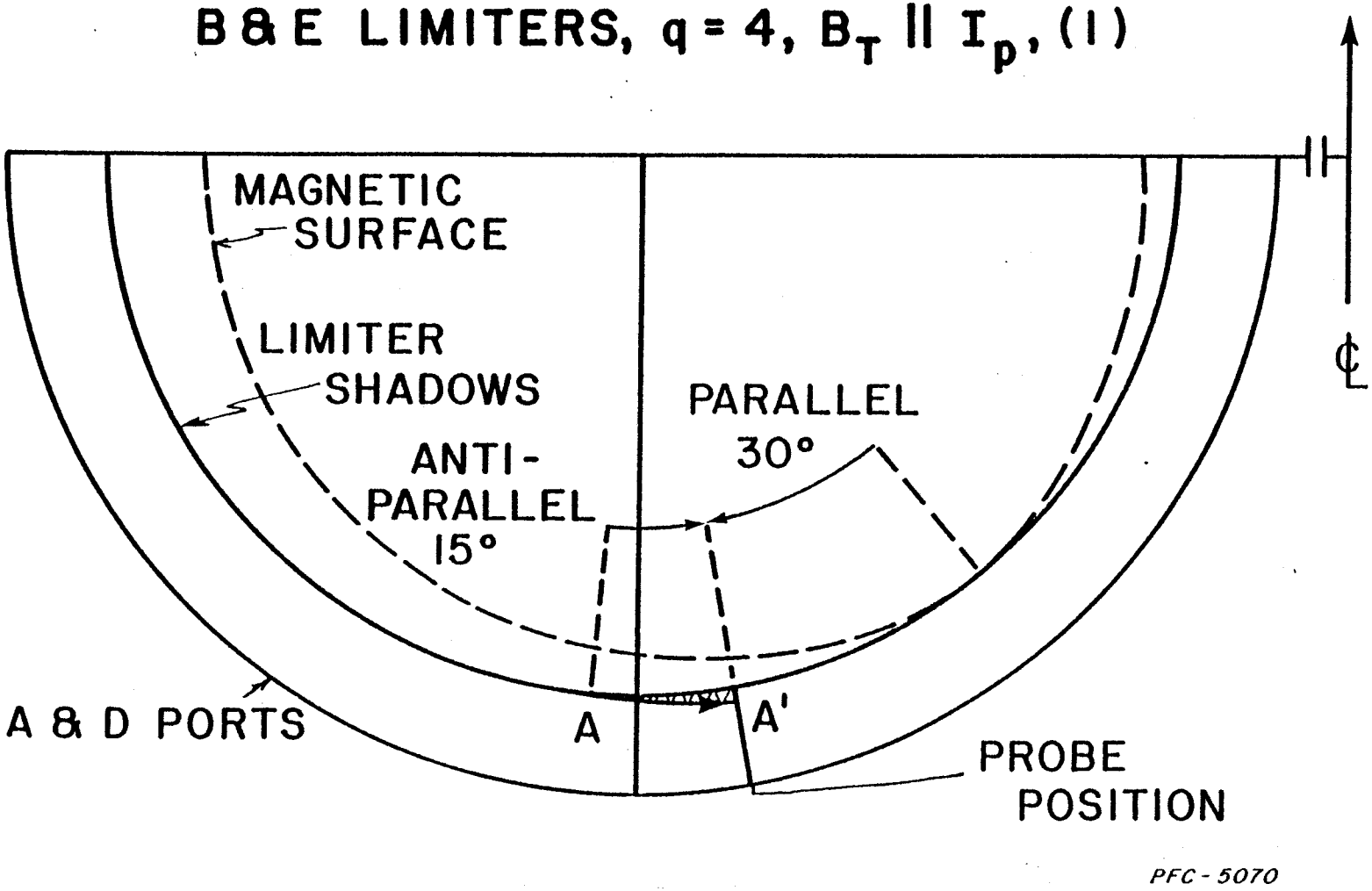
B & E LIMITERS, q = 4, B_T ‖ I_p, (I)
MAGNETIC SURFACE
LIMITER SHADOWS
ANTI-PARALLEL 15°
PARALLEL 30°
A & D PORTS
A
A'
PROBE POSITION
PFC - 5070

FIG. 16

Figure 17

Qualitative mapping of the magnetic surfaces that just miss the limiter at B port onto D port both parallel (30° poloidal rotation assuming q = 4) and anti-parallel (60° poloidal rotation) to the plasma current. The magnetic surfaces qualitatively have the same shape (Fig. 14) as those computed for $B_T \nparallel I_p$.

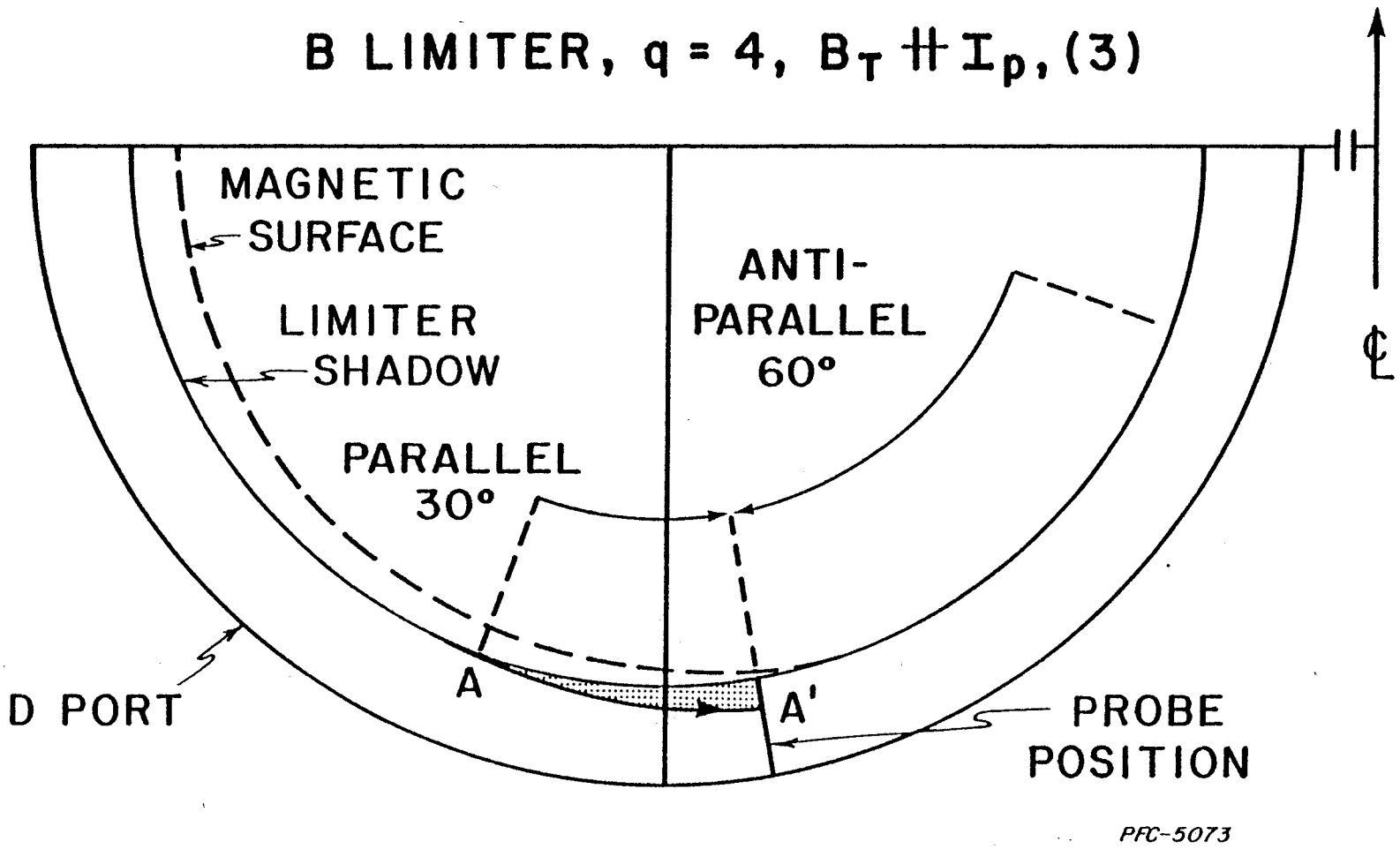
B LIMITER, q = 4, $B_T \parallel I_p$, (3)
MAGNETIC SURFACE
LIMITER SHADOW
PARALLEL 30°
ANTI-PARALLEL 60°
D PORT
A
A'
PROBE POSITION
PFC-5073

FIG. 17

Figure 18

Qualitative mapping of the magnetic surfaces that just miss the limiter at B port onto A port both parallel (75° poloidal rotation assuming q = 4) and anti-parallel (15° poloidal rotation) to the plasma current. The magnetic surfaces qualitatively have the same shape (Fig. 13) as those computed for $B_T \parallel I_p$.

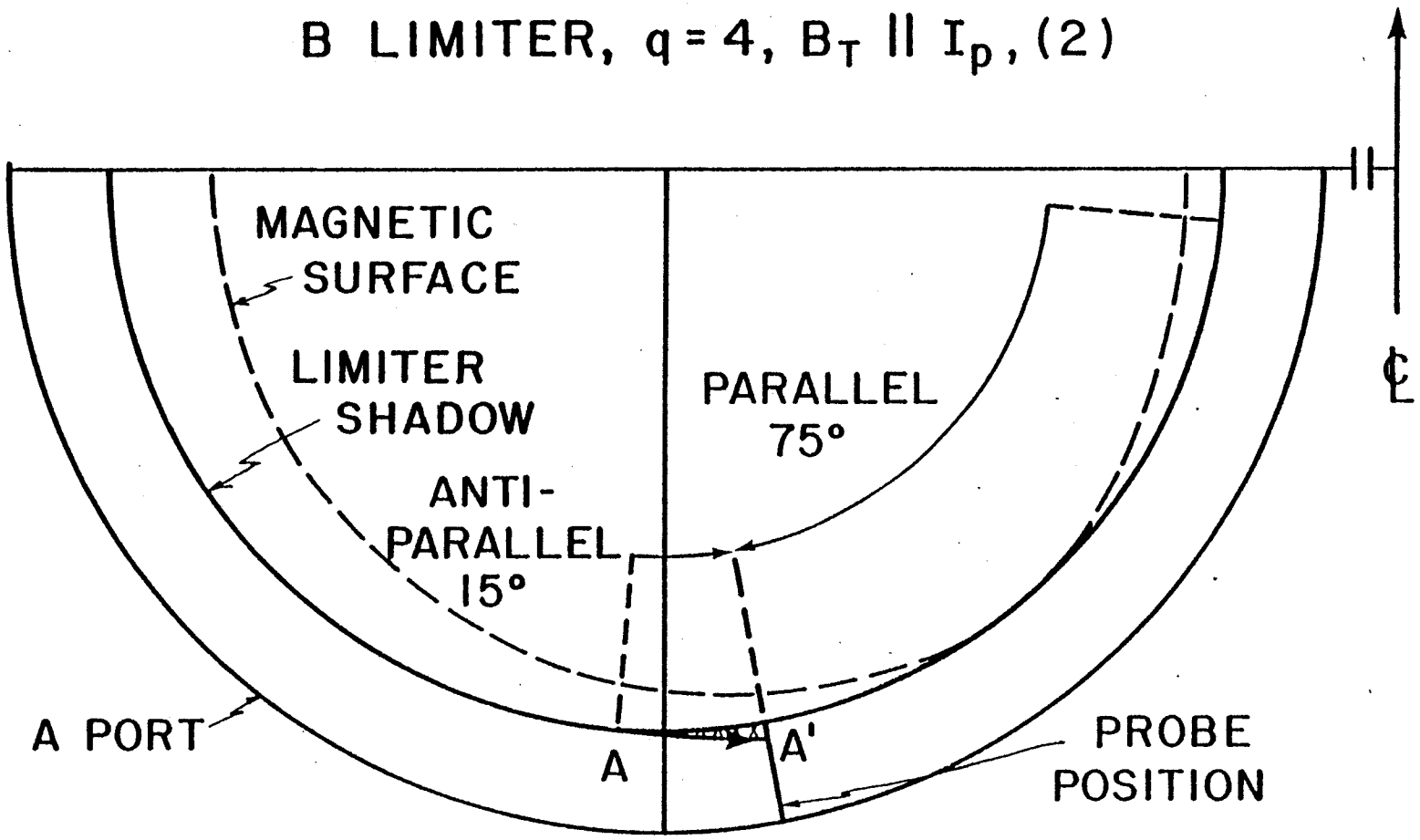
B LIMITER, q = 4, B_T || I_p, (2)
MAGNETIC SURFACE
LIMITER SHADOW
ANTI-PARALLEL 15°
PARALLEL 75°
℄
A PORT
A
A'
PROBE POSITION
PFC-5074

FIG. 18

Figure 19

Qualitative mapping of the magnetic surfaces that just miss the limiter at B port onto A port both parallel (75° poloidal rotation assuming q = 4) and anti-parallel (15° poloidal rotation) to the plasma current. The magnetic surfaces qualitatively have the same shape (Fig. 14) as those computed for $B_T \nparallel I_p$.

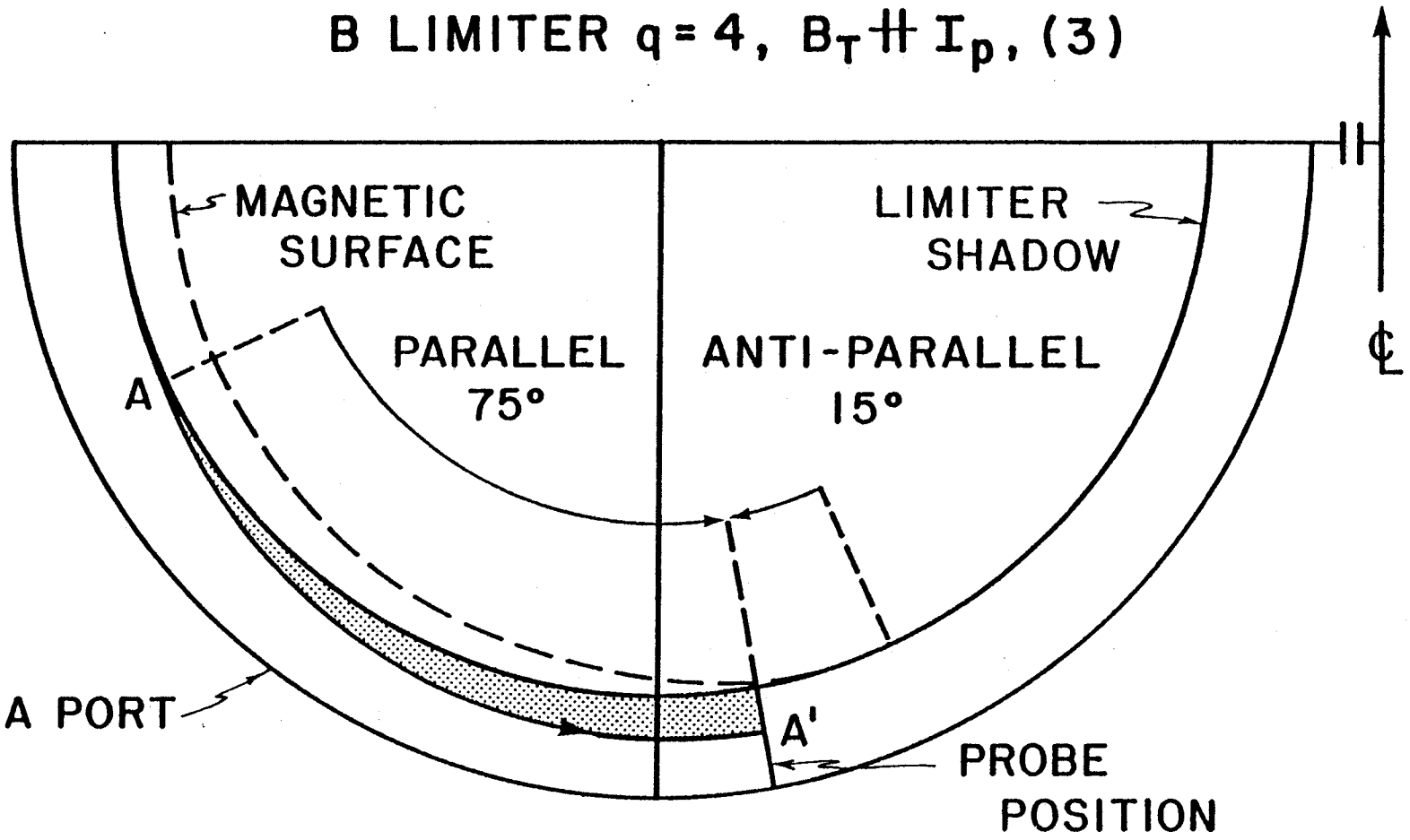
B LIMITER q = 4, $B_T \nparallel I_p$, (3)
MAGNETIC SURFACE
LIMITER SHADOW
PARALLEL 75°
ANTI-PARALLEL 15°
A
A'
A PORT
PROBE POSITION
PFC-5072

FIG. 19

Figure 20

Model showing two density profiles "a" and "b" which results in a density profile "c" with a scrape-off thickness greater than the scrape-off thicknesses for either curves "a" or "b".

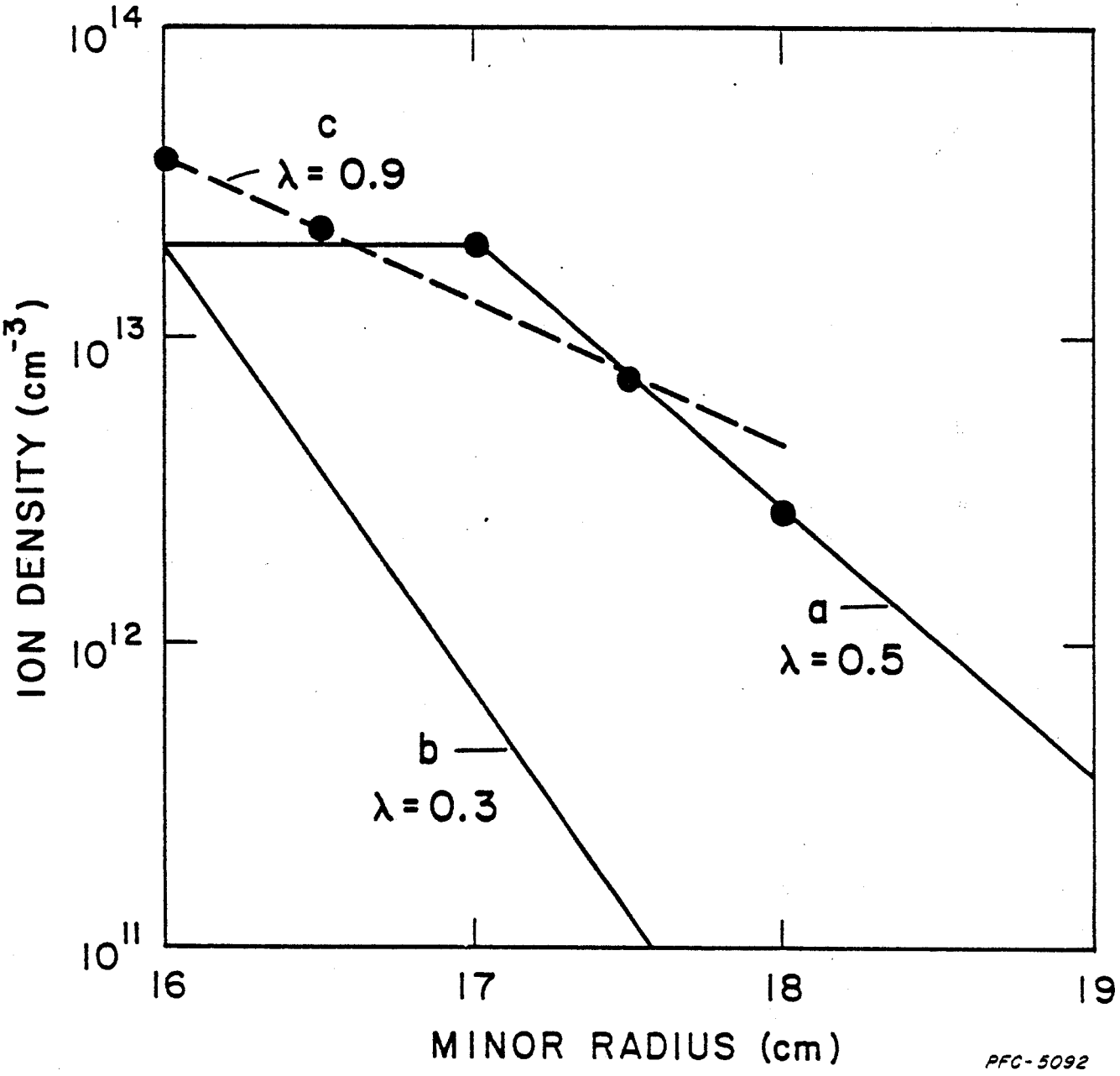
10^{14}
10^{13}
10^{12}
10^{11}
ION DENSITY (cm^{-3})
c
$\lambda = 0.9$
a
$\lambda = 0.5$
b
$\lambda = 0.3$
16
17
18
19
MINOR RADIUS (cm)
PFC-5092

FIG. 20

Figure 21

Qualitative mapping of the magnetic surfaces that just miss the limiters on B and E ports (Fig. 1) onto F port, both parallel (15° poloidal rotation assuming q = 4) and anti-parallel (30° poloidal rotation) to the plasma current. The magnetic surfaces qualitatively have the same shape (Fig. 13) as those computed for $B_T \parallel I_p$. Neglecting diffusion, it can be seen that the magnetic surfaces carry the plasma either out beyond the limiter shadow (A to A') or further into the body of the plasma at F port depending on the poloidal location and direction of the thermal flux. This results in the ratio of the anti-parallel to parallel thermal fluxes being > 1 at points D and F, and the thermal flux being carried out further at point E than both D and F.

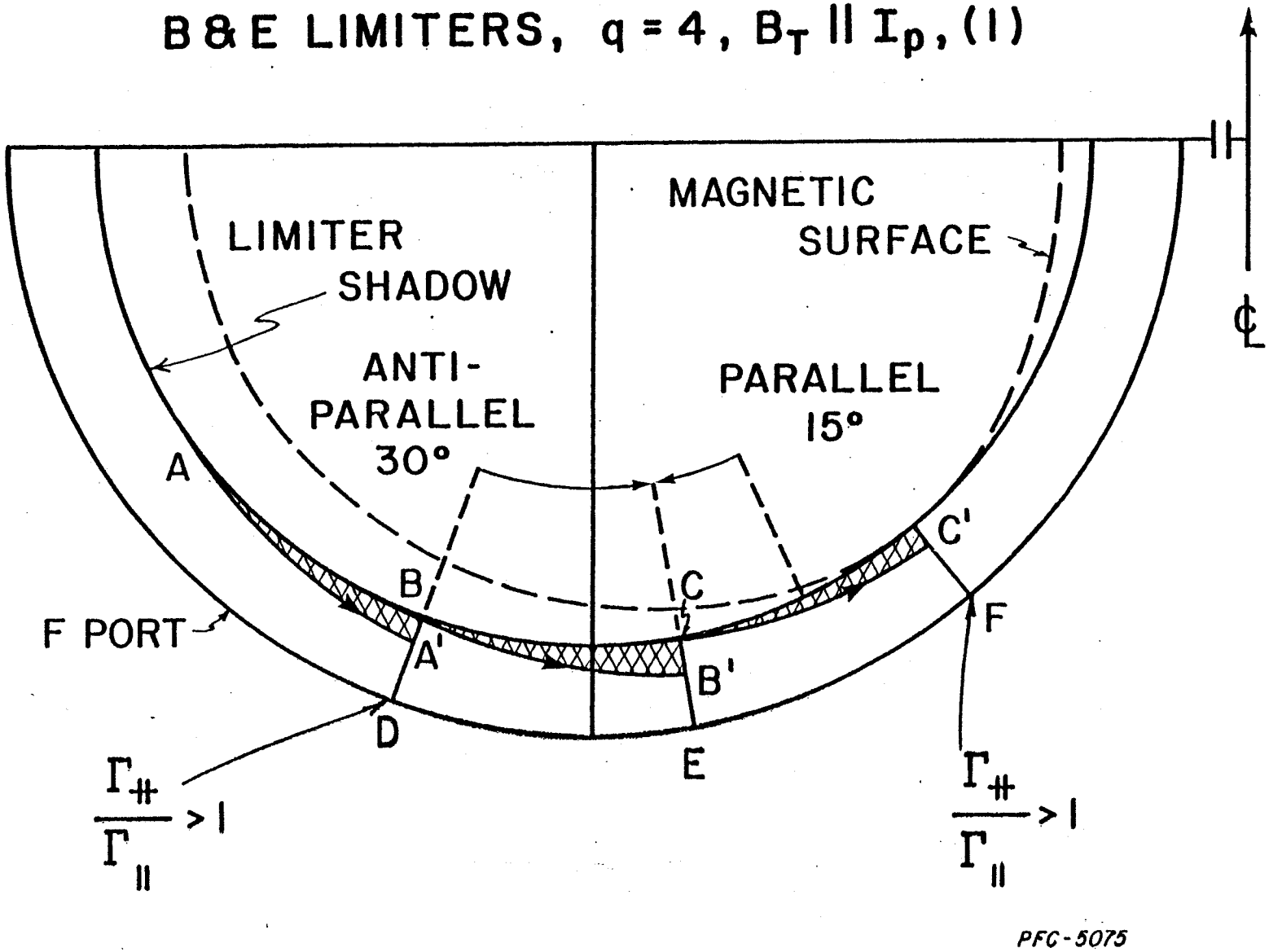
B&E LIMITERS, q = 4, $B_T \parallel I_p$, (1)
LIMITER SHADOW
MAGNETIC SURFACE
ANTI-PARALLEL 30°
PARALLEL 15°
A
B
C
C'
A'
B'
D
E
F
F PORT
$\frac{\Gamma_{\perp}}{\Gamma_{\parallel}} > 1$
$\frac{\Gamma_{\perp}}{\Gamma_{\parallel}} > 1$
PFC-5075

FIG. 21

Figure 22

Qualitative mapping of the magnetic surfaces that just miss the limiter at B port onto F port, both parallel (60° poloidal rotation assuming q = 4) and anti-parallel (30° poloidal rotation) to the plasma current. The magnetic surfaces qualitatively have the same shape (Fig. 13) as those computed for $B_T \parallel I_p$. Neglecting diffusion, it can be seen that the magnetic surfaces carry the plasma either out beyond the limiter shadow (A to A') or further into the body of the plasma at F port, depending on the poloidal location and direction of the thermal flux. This results in the ratio of the anti-parallel to parallel thermal fluxes being > 1 at point E and ≈ 1 and G, and the thermal flux being carried out further at point F than both E and G.

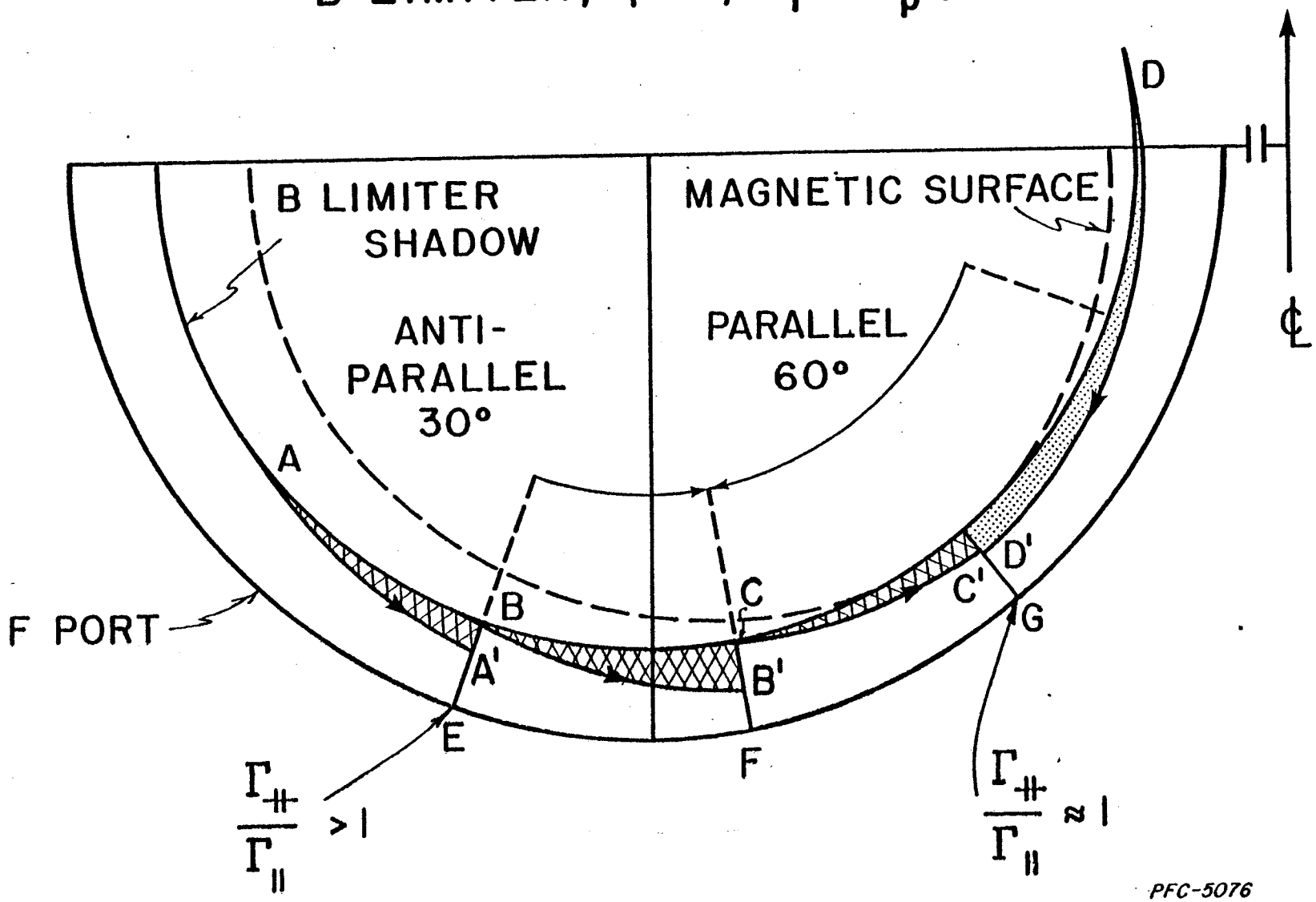
B LIMITER, q = 4, $B_T \parallel I_p$, (2)
B LIMITER SHADOW
MAGNETIC SURFACE
ANTI-PARALLEL 30°
PARALLEL 60°
D
A
B
C
C'
D'
G
A'
B'
E
F
F PORT
$\frac{\Gamma_{+\parallel}}{\Gamma_{\parallel}} > 1$
$\frac{\Gamma_{+\parallel}}{\Gamma_{\parallel}} \approx 1$
PFC-5076

FIG. 22

Figure 23

Qualitative mapping of the magnetic surfaces that just miss the limiter at B port onto F port, both parallel (60° poloidal rotation assuming q = 4) and anti-parallel (30° poloidal rotation) to the plasma current. The magnetic surfaces qualitatively have the same shape (Fig 14) as those computed for $B_T \parallel I_p$. Neglecting diffusion, it can be seen that the magnetic surfaces carry the plasma either out beyond the limiter shadow (A to A') or further into the body of the plasma at F port, depending on the poloidal location and direction of the thermal flux. This results in the ratio of the parallel to anti-parallel thermal fluxes being > 1 at points D and F.

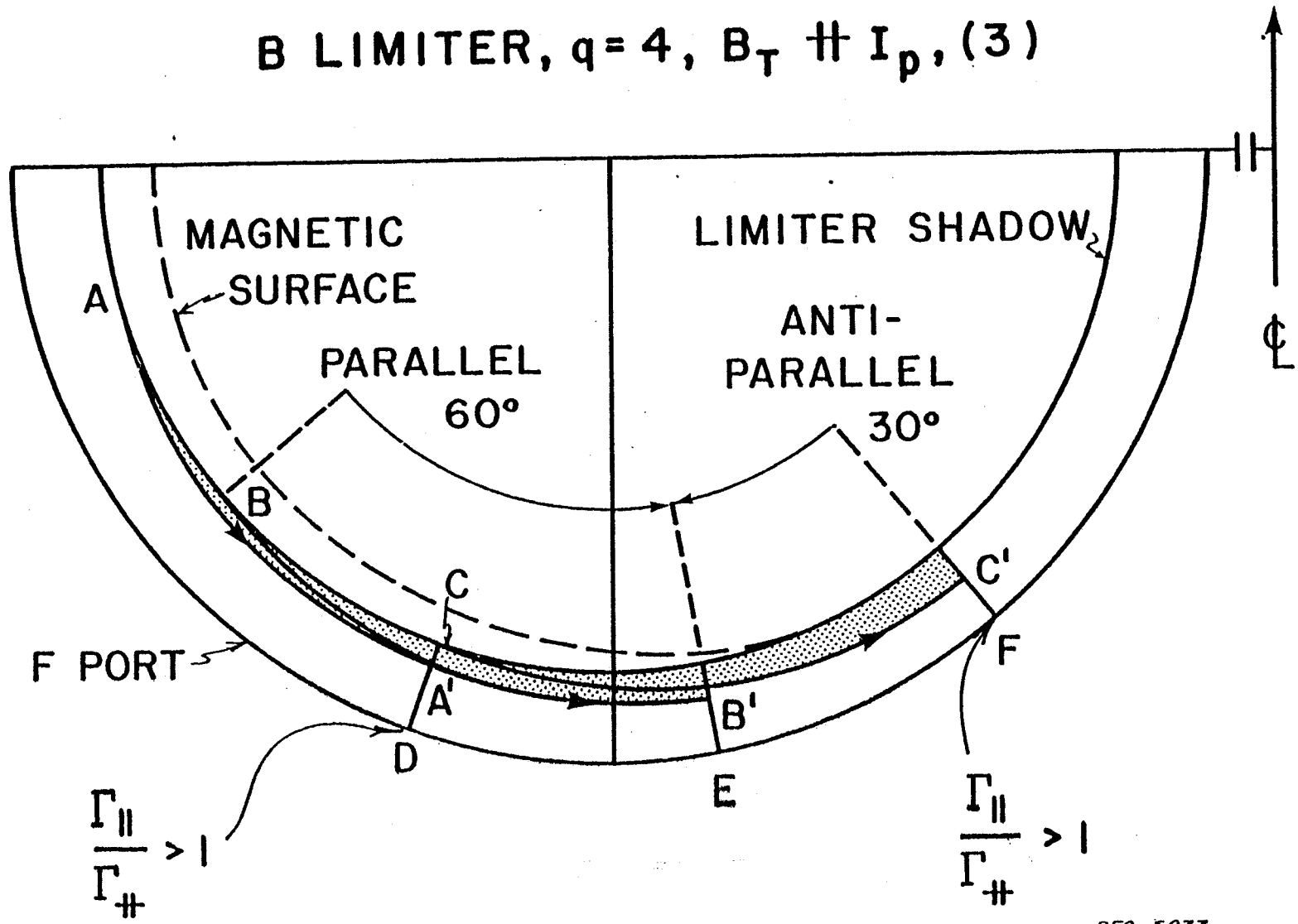
B LIMITER, q= 4, B_T ∦ I_p, (3)
MAGNETIC SURFACE
LIMITER SHADOW
ANTI-PARALLEL 30°
PARALLEL 60°
A
B
C
C'
F
F PORT
A'
B'
D
E
$\frac{\Gamma_{\parallel}}{\Gamma_{\perp}} > 1$
$\frac{\Gamma_{\parallel}}{\Gamma_{\perp}} > 1$
PFC-5077

FIG. 23

Figure 24

Model showing the ratio of the two thermal flux profiles parallel and anti-parallel to the plasma current.

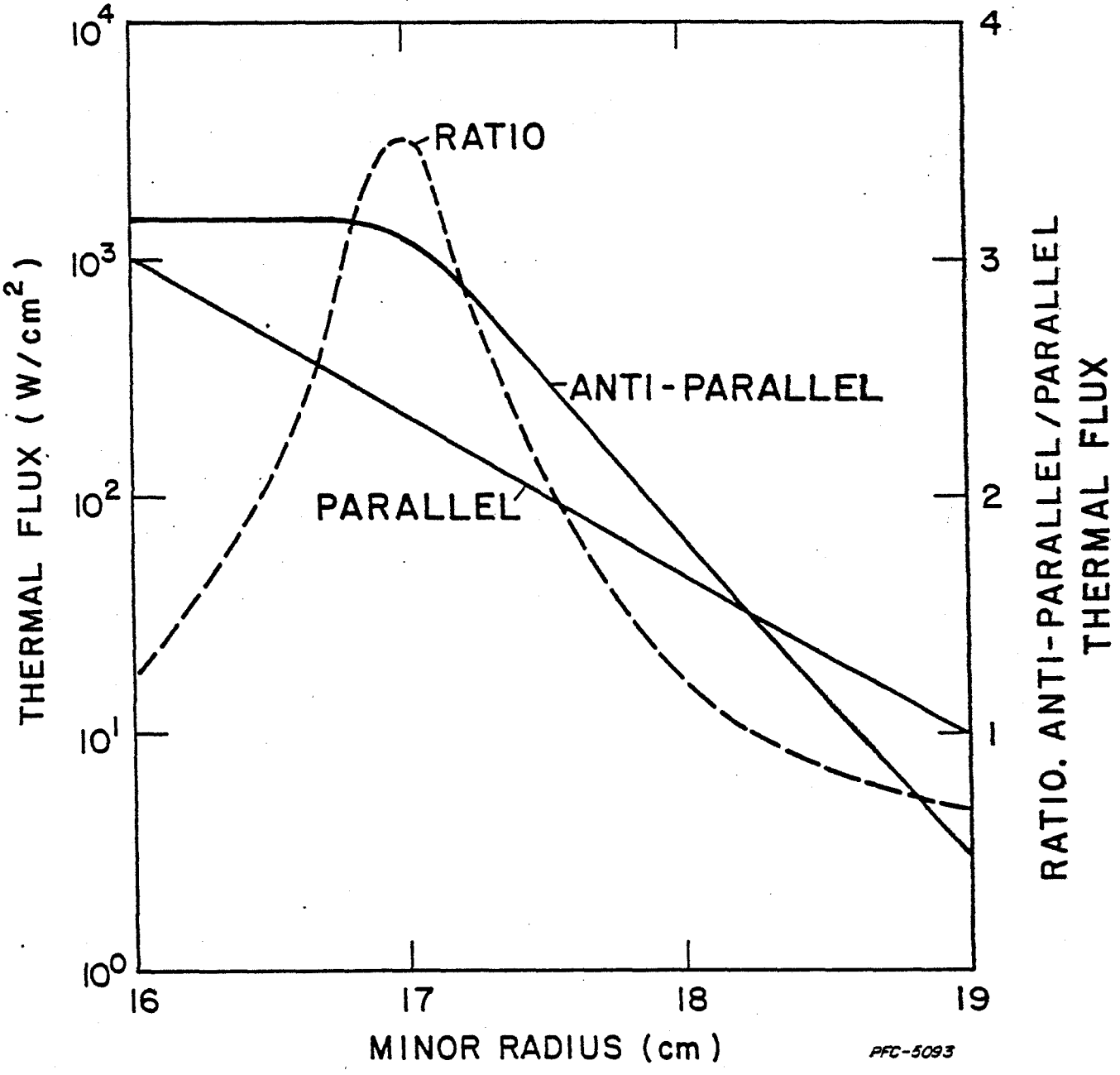
RATIO
ANTI-PARALLEL
PARALLEL
THERMAL FLUX (W/cm^2)
RATIO, ANTI-PARALLEL/PARALLEL THERMAL FLUX
MINOR RADIUS (cm)
10^4
10^3
10^2
10^1
10^0
16
17
18
19
4
3
2
1
PFC-5093

FIG. 24